

# General complex rotated finite-element method for predissociation studies of diatomic molecules: An application on the $(1-6)^1\Sigma_g^+$ states of $H_2$

Stefan Andersson and Nils Elander

*Department of Physics, Stockholm Center for Physics, Astronomy, and Biotechnology, SE-10691 Stockholm, Sweden*

(Received 27 November 2003; published 18 May 2004)

An exterior complex rotated finite element method was applied on the diabatic multichannel Schrödinger equation in order to compute and compare rovibronic energy structures, predissociation widths, and nonradiative lifetimes for levels in the  $(1-4)$ ,  $(1-5)$ , and  $(1-6)^1\Sigma_g^+$  manifolds of  $H_2$ . The rotationless ( $v, J=0$ ) levels are found to be more or less shifted relative to each other when comparing the results for these three manifolds. The existence of homogeneous spectroscopic perturbations was investigated by studying the rovibronic ( $v, J=0-10$ ) sequences for energies and level widths. Known experimental and theoretical radiative lifetimes were used to estimate present levels that might be spectroscopically measurable. The computed level widths for the *EF*, *GK*, and *H* electronic levels were generally found to be about two orders of magnitude larger than previously reported [P. Quadrelli, K. Pressler, and L. Woiniewicz, *J. Chem. Phys.* **93**, 4958 (1990)], indicating a somewhat stronger predissociation.

DOI: 10.1103/PhysRevA.69.052507

PACS number(s): 33.20.Vq, 34.50.-s

## INTRODUCTION

In theoretical studies of diatomic molecules one frequently takes into account two or more close-lying potential-energy curves (PECs) of electronic states, having the same spin and symmetry, correlating with different dissociation limits. In the adiabatic representation, these PECs do not cross each other [1], and in the region of avoided intersections nonadiabatic effects are likely to be important.

Interactions between bound levels and the continuum give rise to bond breaking phenomena in the form of predissociation. The variation of the fragmentation width of close-lying levels can be quite dramatic. The main fragmentation flow in a particular energy region can sometimes be located to only a few rotational levels. It is thus interesting to study these phenomena in some detail.

In systems of singlet states in light molecules, such as excited  $^1\Sigma_g^+$  states of molecular hydrogen  $H_2$  [3,2,4], the first derivative coupling elements  $B_{ij}(R) = \langle i | \nabla_R | j \rangle$ , between electronic states  $|i\rangle$  and  $|j\rangle$ , are the dominating mechanism among all of the possible predissociation processes [5]. Thus, vibronically bound states, embedded in the continuum of lower-lying PECs, may undergo nonradiative transitions resulting in a broadening of the energy levels.

The adiabatic multichannel Schrödinger equation can be difficult to solve numerically [6]. An alternative approach is to form a diabatic, or approximately diabatic, basis through an orthogonal transformation [7]. This generally simplifies the computations, particularly in the region of strongly avoided intersections where the  $B_{ij}(R)$  elements are often rapidly varying, with respect to both magnitude and sign. We here refer to a strictly diabatic basis as a representation for which all derivative couplings in the multichannel Schrödinger equation are removed [7]. This is generally difficult to accomplish, even if it is theoretically straightforward for a diatomic system [7]. The problem is that, in numerical applications, only a finite number of PECs are included in the calculations. Thus, when we here speak about a diabatic

basis it is understood that the representation is diabatic within the set of electronic states taken into account in the approximation.

The rovibronic energy-level structure of excited states in  $H_2$  has been the subject of several experimental [8–10] and theoretical [11,3,12] studies, while predissociation studies of these levels are more rare. Using *ab initio* wave functions, Quadrelli *et al.* [2] calculated energy shifts, level widths, and nonradiative lifetimes for the first three excited rovibronic  $^1\Sigma_g^+$  states of  $H_2$  generated by nonadiabatic coupling with the electronic ground state. According to their results, excited rovibronic  $^1\Sigma_g^+$  levels in  $H_2$  are more or less predissociated. Therefore, it would be interesting to further investigate this mechanism, applying another approach. We have previously used an exterior complex rotated one-dimensional finite element method to study  $CO^{2+}$  [13], CaH [14],  $B_2$  [15], and  $Al_2$  [16]. In this approach we compute the energy and width of an individual level as one complex-valued energy [17–21]. Both the obtained energy and width are thus converged results. This should be compared with the golden rule treatment of Quadrelli *et al.* [2]. Here the real part of the energy and the real valued wave function are first obtained and then used to compute the width. This means that the wave function and the real part of the energy in principal have to be perturbed and shifted in order to account for the predissociation process. Our previous experience [13–16] is that the energies and, in particular, the level widths are always more or less shifted when compared with results based on the golden rule approach. Furthermore, in these calculations, which were based on a complex rotated finite element method, convergence was always reached for the real energies as well as for the level widths. Therefore, we have reasons to believe that the golden rule approach may not always be convenient to apply on theoretical predissociation problems. This motivates us to use our method also in the present study.

Using data of Woiniewicz [22], Quadrelli *et al.* [2], and Woiniewicz and Dressler [4], we here apply a general

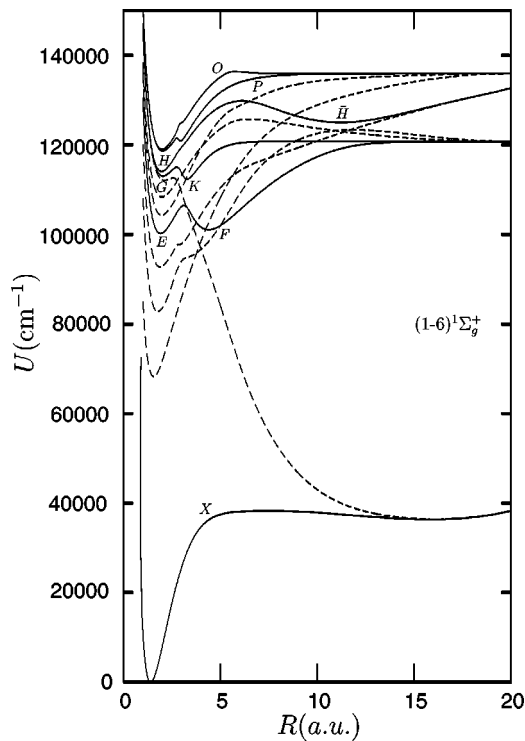


FIG. 1. Adiabatic (solid lines) and diabatic (dashed lines) electronic potential-energy curves for the  $(1-6) \ ^1\Sigma_g^+$  manifold of  $H_2$ .

Runge-Kutta-Fehlberg (RKF45) (in fourth order with fifth order correction) procedure to transform the adiabatic  $(1-6) \ ^1\Sigma_g^+$  states of  $H_2$  to a diabatic representation (See. Fig. 1). Then a multichannel Schrödinger equation is formed, which is numerically solved by means of a complex rotated one-dimensional finite element method, in order to compute rovibronic term energy values, predissociation widths, and nonradiative lifetimes of excited levels.

Following Herzberg [23], the  $1, 2, \dots, 6 \ ^1\Sigma_g^+$  states will here be denoted as  $X, EF, GK, H\bar{H}, P,$  and  $O,$  respectively, when separate states are considered, while the number representation is used for manifolds of states, i.e.,  $(1-4), (1-5),$  and  $(1-6) \ ^1\Sigma_g^+$  for the 4-, 5-, and 6-state approximation, respectively.

The ground-state Born-Oppenheimer (BO) PEC was taken from Wolniewicz [22], while the first five excited  $^1\Sigma_g^+$  BO PECs, adiabatic corrections, and nonadiabatic coupling elements were obtained from the highly accurate *ab initio* calculations of Wolniewicz and Dressler [4]. Elements for the coupling of the  $EF, GK,$  and  $H \ ^1\Sigma_g^+$  states with the ground state were taken from Quadrelli *et al.* [2], while the corresponding couplings for the  $O$  and  $P \ ^1\Sigma_g^+$  states are missing. However, assuming these to be relatively weak, they were here neglected.

There are several reasons for undertaking the present work.

(i) To test a general method for predissociation studies of diatomic  $n$ -channel problems, where  $n$  is an arbitrary positive integer.

(ii) To investigate the difference in our treatment and the bound state + golden rule formalism of Quadrelli *et al.*

(iii) To study how term energy values and level widths are influenced by close-lying  $^1\Sigma_g^+$  states, and to compare results for approximations containing four, five, and six electronic states.

Our theoretical approach is described in Sec. I, where the multichannel Schrödinger problem is outlined in Secs. I A and I B. Our numerical approach, based on the Runge-Kutta-Fehlberg technique and a one-dimensional finite element method, is discussed in Sec. II. Our input data and its limitations are discussed in Sec. III. In Sec. IV our calculations are briefly described. Presentation and discussion of results are found in Sec. V. The last section summarizes the paper.

## I. THEORY

All formulas and equations in this section are expressed in atomic units (a.u.) unless stated otherwise.

### A. The multichannel Schrödinger equation

Consider a diatomic molecule with nuclear masses  $M_A$  and  $M_B$ . Nuclear and electronic coordinates are denoted by  $R$  and  $\mathbf{r}$ , respectively. The total nonrelativistic Hamiltonian in the center of mass system is

$$H = H^{(0)} - \frac{1}{2\mu} \nabla_R^2 - \frac{1}{8\mu} \left( \sum_j \nabla_{r_j} \right)^2 - \frac{1}{2\mu_\alpha} \nabla_R \cdot \sum_j \nabla_{r_j}, \quad (1)$$

where  $R = |\mathbf{R}_A - \mathbf{R}_B|$ ,  $H^{(0)}$  is the clamped-nuclei Hamiltonian, and

$$\mu = \frac{M_A M_B}{M_A + M_B}, \quad \mu_\alpha = \frac{M_A M_B}{M_A - M_B}. \quad (2)$$

For a homonuclear diatomic system the last term in Eq. (1), which is responsible for the  $g$ - $u$  symmetry breaking, disappears. Thus, the Hamiltonian for a two-electron system, such as  $H_2$ , now takes the form

$$H = H^{(0)} + H^{(1)} + H^{(2)} + H^{(3)}, \quad (3)$$

where

$$H^{(1)} = -\frac{1}{2\mu} \nabla_R^2, \quad (4)$$

$$H^{(2)} = -\frac{1}{8\mu} (\nabla_{r_1}^2 + \nabla_{r_2}^2), \quad (5)$$

$$H^{(3)} = -\frac{1}{4\mu} \nabla_{r_1} \cdot \nabla_{r_2}. \quad (6)$$

Here,  $H^{(1)}$  is the relative kinetic-energy operator for the nuclei,  $H^{(2)}$  is the kinetic-energy correction for the electrons, and  $H^{(3)}$  is the mass polarization correction.

The  $H^{(1)}, H^{(2)},$  and  $H^{(3)}$  terms form the nuclear-mass-dependent Hamiltonian

$$H' = -\frac{1}{2\mu} (\Delta_R + G), \quad (7)$$

with the nuclear Laplacian [4],

$$\Delta_R = \frac{1}{R^2} \frac{d}{dR} \left( R^2 \frac{d}{dR} \right) - \frac{L_+ L_- - \Lambda(\Lambda + 1)}{R^2}, \quad (8)$$

where  $L_{\pm} = L_x \pm iL_y$  refer to the molecule-fixed frame, and where  $\Lambda$  is the eigenvalue of the angular-momentum operator  $L_z$  within blocks of electronic states belonging to the same symmetry species (+ or -) [4]. The second term in Eq. (7),

$$G = \frac{1}{4} (\nabla_{r_1} + \nabla_{r_2})^2, \quad (9)$$

is formed by the correction terms  $H^{(2)}$  and  $H^{(3)}$ .

The adiabatic corrections to the BO PECs come from the diagonal elements [4],

$$\langle i | H' | i \rangle = -\frac{1}{2\mu} \langle i | \Delta_R + \frac{1}{4} (\nabla_{r_1} + \nabla_{r_2})^2 | i \rangle. \quad (10)$$

A method for calculating these corrections is described in Ref. [24].

In order to obtain nonadiabatic couplings between different electronic states, we form an expansion

$$\Psi(R, \mathbf{r}) = \frac{1}{R} \sum_{j=1}^n \phi_j(R, \mathbf{r}) \chi_j(R) = \frac{1}{R} \boldsymbol{\phi}(R, \mathbf{r}) \cdot \boldsymbol{\chi}(R), \quad (11)$$

where  $\phi_j(R, \mathbf{r})$  are electronic wave functions. The upper limit  $n$  of the truncated sum denotes the total number of electronic states included in the approximation. The expansion coefficients  $\chi_j(R)$  represent the nuclear motion governed by the nonadiabatic multichannel Schrödinger equation,

$$-\frac{1}{2\mu} \left( \frac{d^2 \chi_i(R)}{dR^2} + \sum_{j=1}^n \left[ A_{ij}(R) + 2B_{ij}(R) \frac{d}{dR} \right] \chi_j(R) \right) + U_{ii}^J(R) \chi_i(R) = E_{vJ} \chi_i(R), \quad (12)$$

or in matrix form,

$$\left[ -\frac{1}{2\mu} \left( \mathbf{I} \frac{d^2}{dR^2} + \mathbf{A}(R) + 2\mathbf{B}(R) \frac{d}{dR} \right) + \mathbf{U}^J(R) \right] \boldsymbol{\chi}(R) = \mathbf{I} E_{vJ} \boldsymbol{\chi}(R). \quad (13)$$

The corresponding matrix elements are

$$A_{ij}(R) = \left\langle i \left| \frac{d^2}{dR^2} - \frac{L_+ L_- - \Lambda(\Lambda + 1)}{R^2} + G \right| j \right\rangle, \quad (14)$$

$$B_{ij}(R) = -B_{ji}(R) = \left\langle i \left| \frac{d}{dR} \right| j \right\rangle, \quad (15)$$

$$U_{ii}^J(R) = \langle i | H^{(0)} | i \rangle + \frac{J(J+1)}{\mu R^2}. \quad (16)$$

The second-order derivative coupling included in  $A_{ij}(R)$  is symmetric, i.e.,

$$D_{ij}(R) = D_{ji}(R) = \left\langle i \left| \frac{d^2}{dR^2} \right| j \right\rangle. \quad (17)$$

## B. A diabatic representation of the multichannel Schrödinger equation

It is well known that the nonadiabatic couplings in Eq. (13) may produce numerical difficulties [6]. This is particularly the case for the  $B_{ij}(R)$  elements which are usually varying rapidly, both with respect to magnitude and sign. Furthermore, the coupled differential equations (13) are of second order, also including first derivatives [25,26]. However, these complications are commonly avoided by making an orthogonal transformation to a diabatic (d) basis set [7],

$$\boldsymbol{\phi}(R, \mathbf{r}) = \boldsymbol{\phi}^{(d)}(R, \mathbf{r}) \mathbf{T}^T(R), \quad (18)$$

where  $\mathbf{T}(R)$  and  $\mathbf{T}^T(R)$  are the transformation matrix and its transpose, respectively. In order to preserve the total wave function in Eq. (11) the nuclear wave functions are transformed as

$$\boldsymbol{\chi}(R, \mathbf{r}) = \mathbf{T}(R) \boldsymbol{\chi}^{(d)}(R, \mathbf{r}). \quad (19)$$

A diabatic Schrödinger equation is obtained by substituting the diabatic representation (19) into Eq. (13). By doing so, a second-order differential equation, including first derivatives, is obtained. It is desirable to get rid of the first derivative terms  $d\boldsymbol{\chi}^{(d)}(R)/dR$  in Eq. (13). This requires that the condition

$$\frac{d}{dR} \mathbf{T}(R) + \mathbf{B}(R) \mathbf{T}(R) = \mathbf{0} \quad (20)$$

is fulfilled [15,16,27], which implies that  $\mathbf{T}(R)$  is orthogonal [28]. Assuming

$$\lim_{R \rightarrow \infty} \mathbf{B}(R) = 0 \Rightarrow \lim_{R \rightarrow \infty} \mathbf{T}(R) = \mathbf{I}, \quad (21)$$

one obtains a boundary condition to Eq. (20). Thus, by solving Eq. (20), together with the boundary condition (21), unique solutions of a diabaticization problem for any number of coupled equations can be obtained [16].

By substitution to the diabatic representation, the Schrödinger equation (13) transforms to

$$\left\{ -\frac{1}{2\mu} \left[ \frac{d^2}{dR^2} - \frac{J(J+1)}{R^2} \right] \mathbf{I} + \mathbf{U}^{(d)}(R) \right\} \mathbf{T}(R) \boldsymbol{\chi}^{(d)}(R) = E_{vJ} \mathbf{T}(R) \boldsymbol{\chi}^{(d)}(R). \quad (22)$$

By working out the differentials in Eq. (22), multiplying from the left by  $\mathbf{T}^T(R)$ , and using Eq. (20), it is in general straightforward to derive an expression for the diabatic potential-energy matrix representing a manifold of only  $\Sigma_g^+$  electronic states [27]:

$$\mathbf{U}^{(d)}(R) = \mathbf{T}^T \left[ \mathbf{U}(R) - \frac{1}{2\mu} \{ \mathbf{A} - \mathbf{B}^2 - \nabla \mathbf{B} \} \right] \mathbf{T}, \quad (23)$$

where the matrix elements of  $\mathbf{A}(R)$  are calculated as sums consisting of two parts [4],  $A_{ij}(R) = \Delta_{ij}(R) + G_{ij}(R)$ , with

$$\Delta_{ij}(R) = \left\langle i \left| \frac{d^2}{dR^2} - \frac{L_+ L_- - \Lambda(\Lambda + 1)}{R^2} \right| j \right\rangle, \quad (24)$$

$$G_{ij} = \frac{1}{4} \langle i | \nabla_1 + \nabla_2 | j \rangle. \quad (25)$$

The elements  $\Delta_{ij}(R)$  are neither symmetric nor antisymmetric;  $G_{ij}(R)$  are symmetric. In practice, it may happen that the chosen electronic basis set is not accurately orthogonal. Consequently, the functions  $B_{ij}(R)$  are not mutually antisymmetric with respect to interchanges of  $\phi_i(R, \mathbf{r})$  and  $\phi_j(R, \mathbf{r})$ . It is therefore convenient to form the antisymmetric coupling matrix

$$\mathbf{B}^a(R) = \frac{1}{2} [\mathbf{B}(R) - \mathbf{B}^T(R)], \quad (26)$$

having the elements

$$B_{ij}^a(R) = \frac{1}{2} [B_{ij}(R) - B_{ji}(R)]. \quad (27)$$

It is further known [29] that the first derivative coupling functions have the property

$$\frac{d}{dR} B_{ij}^a(R) = \frac{1}{2} [A_{ij}(R) - A_{ji}(R)] = A_{ij}^a(R). \quad (28)$$

For a nonorthogonal basis set we apply Eq. (23) and substitute  $dB_{ij}^a(R)/dR$  by  $A_{ij}^a(R)$ . From the known relation

$$A_{ij}(R) = A_{ij}^s(R) + A_{ji}^a(R), \quad (29)$$

we then form the symmetric matrix  $\mathbf{A}^s(R)$ , with elements  $A_{ij}^s(R) = A_{ij}(R) - A_{ji}^a(R)$ . Thus, in the case of a nonorthogonal basis set the diabatic potential-energy matrix  $\mathbf{U}^{(d)}(R)$  is transformed as [27]

$$\mathbf{U}^{(d)}(R) = \mathbf{T}^T \left[ \mathbf{U}(R) - \frac{1}{2\mu} [\mathbf{A}^s - \mathbf{B}^2] \right] \mathbf{T}, \quad (30)$$

### C. Exterior complex scaling

Eigenvalue problems containing bound levels and resonances may be solved by using complex scaling (CS) methods [17–21]. The complex energy, which is composed of the real energy and the width of a level, is then a solution of a non-Hermitian complex symmetric analytic continuation of a nondilated Hermitian Schrödinger problem. The original uniform CS, suggested by Balslev and Combes [17,18], requires the potential  $V(R)$  to be analytic in the entire domain  $[R_{min}, R_{max}]$ . However, when  $V(R)$  is represented by a set of discrete points, an alternative in the form of the exterior complex scaling (ECS) can be used [30–32]. In the ECS the radial coordinates are scaled as

$$R \rightarrow \begin{cases} R, & R \leq R_s \\ R_s + (R - R_s)e^{i\theta}, & R > R_s. \end{cases} \quad (31)$$

Here  $R_s$  is the exterior scaling radius up to which the potentials are real while the outer part,  $R > R_s$  is analytically continued. The ECS requirement is that only  $V(R)$  for  $R > R_s$  needs to be a function that can be analytically continued. The potential in the inner region  $R \leq R_s$  may in fact be described only by discrete numerical values. The ratio between the energies and their widths in the present problem is so large that extreme care of the numerical procedures need to be

taken. This thus forced us to replace the previously discussed sharp exterior complex scaling by the, computationally more demanding but more accurate, smooth exterior complex scaling [33]. Here

$$R \rightarrow R + \Lambda g(R), \quad \Lambda = e^{i\phi} - 1, \quad (32)$$

with

$$g(R) = \begin{cases} 0, & R \leq R_s \\ (R - R_s)(1 - e^{\sigma(R - R_s)^2}), & R > R_s, \end{cases} \quad (33)$$

where  $\sigma$  is the curvature parameter, and both the function and its derivative are continuous in  $R_s$ . In other words, the sharp bend at the point  $R_s$  is replaced by a smooth continuation such that all terms in the Haimiltonian are continuous with respect to  $R$ . The accuracy of the calculation then depends on the density of that point grid.

## II. NUMERICAL APPROACH

### A. Computational diabatization

Equations (20) and (21) give us a formal tool and a computational possibility to uniquely obtain a set of diabatic PECs for an arbitrary adiabatic PEC matrix  $\mathbf{U}^{(a)}(R)$ .

Using a matrix version of the RKF45 method [34–36], we are able to propagate  $\mathbf{T}(R)$  in the interval from  $R_{max}$  to  $R_{min}$ . The RKF45 method has a built-in error estimate which allows us to control the accuracy of our calculated matrix  $\mathbf{T}(R)$  to only depend on the word length of the used computer code.

### B. A one-dimensional finite element method

The basic idea of the finite element method (FEM) is to discretize the solution region into a finite number of subregions. The total trial wave function is expanded in a finite element basis,

$$\tilde{\Psi}(R) = \sum_{ij} c_{ij} f_{ij}(R), \quad (34)$$

where it is assumed that smooth ECS has been used. The complex valued,  $\phi$ -dependent expansion coefficients,  $c_{ij}$  are defined within each element and restricted through continuity conditions for  $\tilde{\Psi}(R)$  over element boundaries [37]. The local basis functions  $f_{ij}$  are nonzero only inside a given element  $i$ ,

$$f_{ij}(R) \equiv 0 \quad \text{for } R \notin [R_{i-1}, R_i], \quad i = 1, \dots, K. \quad (35)$$

The Rayleigh-Ritz variational principle [38] provides an estimate to the complex resonance energies,  $\tilde{\epsilon}_k$  which are obtained as eigenvalues of  $\langle \tilde{\Psi} | H | \tilde{\Psi} \rangle$ , and they are evaluated by solving finite-dimensional problems of the form

$$(\tilde{H} - \tilde{\epsilon}_k \tilde{S}) c_k = 0, \quad (36)$$

where

$$(\tilde{H})_{ij, k\ell} = \langle ij | H | k\ell \rangle, \quad (37)$$

$$(\tilde{S})_{ij,k\ell} = \langle ij|k\ell\rangle,$$

with the notation  $|f_{ij}\rangle = |ij\rangle$ , and

$$\tilde{\epsilon}_k = \tilde{E}_k - i\Gamma_k/2. \quad (38)$$

The  $\tilde{H}_{ij,k\ell}$  and  $\tilde{S}_{ij,k\ell}$  elements are identically zero for  $i \neq k$ , and therefore the global matrices  $\tilde{H}$  and  $\tilde{S}$  become banded and relatively sparse [37].

### III. INPUT DATA

By input data we here refer to the diabatic representations used in the finite element calculations. This input was created using initial data from different sources. In order to understand how this might affect the final results, this section gives a detailed description about the numerical treatment of the initial data points.

The reduced mass  $\mu_{\text{H}_2} = 0.503\,637\,435$  a.u. for  $\text{H}_2$  was used in all calculations.

The ground-state BO PEC in the region  $R = 0.6\text{--}8.0$  a.u. was taken from Wolniewicz [22], while the excited  $EF$ ,  $GK$ ,  $H\bar{H}$ ,  $P$ , and  $O\ ^1\Sigma_g^+$  BO energies, adiabatic corrections, and nonadiabatic derivative coupling elements for  $R = 1.00\text{--}20.00$  a.u. were obtained from high-precision *ab initio* results of Wolniewicz and Dressler [4]. The upper limit of  $R$  for the ground-state BO electronic energy needed to be extended and was therefore smoothly extrapolated to its dissociation limit  $D_e = 38\,293.0406\text{ cm}^{-1}$  [22] for out, i.e., at  $R \approx 20$  a.u.

Elements for the couplings of the  $EF$ ,  $GK$ , and  $H\bar{H}\ ^1\Sigma_g^+$  states with the ground state were obtained from Quadrelli *et al.* [2]. Some of these couplings were given for  $R \geq 1.00\text{--}5.00$  a.u., others for  $R \geq 1.00\text{--}6.00$  a.u. Therefore, all couplings were smoothly extrapolated to be zero for  $R = 20.00$  a.u. The corresponding coupling elements for the  $P$  and  $O\ ^1\Sigma_g^+$  states were missing. Assuming these to be relatively weak they were here neglected.

The accuracy of an exterior complex scaled finite element calculation depends on the density of the point grid used before the scaling point, the choice of basis functions, and the degree of these polynomial basis functions. Therefore all initial data for  $R \geq 1.00\text{--}20.00$  a.u. were interpolated by means of tension splines [39] to be represented by a total number of about 1900 points. All PECs were extrapolated to a maximum internuclear distance at  $R_f = 42.00$  a.u.

It is well known that relativistic corrections of the inner and outer minima of the  $EF$  and  $GK$  electronic energies of  $\text{H}_2$  need to be included in high-precision comparisons with observed term values [4]. However, the present paper is mainly focused on predissociation studies, and as the widths are independent of the small energy shift caused by these corrections, they are excluded in the present calculations. Furthermore, when comparing our different multichannel approximations with respect to rovibronic energies, only the relative position of the energies need to be taken into account.

The last step, required to obtain the necessary input, was to create diabatic representations by applying the procedure

TABLE I. Parameters used in the finite element calculations of the 4-, 5-, and 6-channel Schrödinger equation, where  $n(\text{el}_i)$  is the number of elements and  $n(\text{bas}_i)$  is the number of basis functions within each element. The exterior complex scaling point  $R_s$  as well as the most inner,  $R_i$ , and outer,  $R_f$ , mesh points are given in atomic units. The complex scaling angle is given in degrees.

$n(\text{el}_i)$	$n(\text{bas}_i)$	$R_i$	$R_s$	$R_f$	$\phi$
60	13	0.03	19.00	42.00	7.0

described in Sec. I B and II A. For each one of the adiabatic  $(1-4)^1\Sigma_g^+$ ,  $(1-5)^1\Sigma_g^+$ , and  $(1-6)^1\Sigma_g^+$  manifolds, a diabatic matrix  $\mathbf{U}^{(d)}(R)$  was formed by means of Eqs. (23) and (30), depending on whether the initial data were represented by an orthogonal basis set or not. The step length in our numerical diabatization was  $(1 \times 10^{-4})a_0$ , yielding an error estimate  $\approx 2 \times 10^{-11}\text{ cm}^{-1}$ .

The diabatization results for the  $(1-6)^1\Sigma_g^+$  manifold with respect to energies  $U_{ii}^{(d)}(R)$  are shown in Fig. 1. The structure of the diabatic diagonal potential energies and the corresponding interaction potentials (not displayed here) may look rather peculiar and nonphysical. However, the diabatic representation is just a useful mathematical construction for simplifying numerical treatments and should generally not serve as a graphical representation for understanding the physics connected with the problem studied.

### IV. CALCULATIONS

The  $(1-4)^1\Sigma_g^+$ ,  $(1-5)^1\Sigma_g^+$ , and  $(1-6)^1\Sigma_g^+$  manifolds represent four-, five-, and six-state approximations studied in the present paper, respectively. The diabatic potentials  $U_{ii}^d(R)$  and  $U_{ij}^d(R) (i \neq j)$  were used as input to an exterior complex rotated finite element Schrödinger equation solver [37] in order to compute rovibronic structures as well as level widths for the three approximations discussed above. Note that in the diabatic basis, each  $U_{ij}^d(R)$  in one approximation differs slightly from the corresponding element in other approximations. This gives rise to energy shifts when comparing computed rovibronic structures for different manifolds.

The FEM input grids were found to produce convergent results for a relatively small number of elements and local basis functions. The final results are based on a somewhat larger grid, consisting of 60 elements with 13 local basis functions within each element. Details of the FEM input is presented in Table I. The exterior complex scaling point as well as the angle were varied in small steps in order to check stability. For angles  $\phi \approx 5^\circ$  and scaling points  $R_s \geq 12a_0$  the results were stable. According to the table, these parameters were held constant at somewhat larger values during all calculations.

The lower  $R$  limits of the PECs were extrapolated down to  $0.03a_0$  by using a Lennard-Jones fit [40].

### V. RESULTS AND DISCUSSION

The results for the  $(2-6)^1\Sigma_g^+$  excited states reported here were based on best adiabatic PECs [4], while the ground

state was represented by Born-Oppenheimer electronic energies [22]. This inconsistency produced a shift, making direct comparisons between the presented results and observed as well as with other computed results, not definite. Therefore, the minimum of the ground-state potential was set to zero energy. Thus, all our computed energies were shifted upwards by about  $2300 \text{ cm}^{-1}$  relative to observed energies, while the corresponding level widths remained unaffected by this constant shift. This shift is irrelevant in comparisons between our computed energies for different approximations. To be able to compare our results with observed levels we present the energy differences between consecutive vibrational levels instead of the absolute energies themselves.

In the following sections, term energy values, level widths, and nonradiative lifetimes are labeled as  $E_k^s(v, J)$ ,  $\Gamma_k^s(v, J)$ , and  $\tau_k^s(v, J)$ , respectively, where  $v$  denotes vibrational levels,  $J$  is the total angular momentum, the indices  $k=4, 5, 6$  denote what approximation is considered, and  $s = EF, GK, H\bar{H}, P$ , or  $O$  is the state studied within a chosen approximation. Note that when levels are well localized in only one of the  $EF$ ,  $GK$ , and  $H\bar{H}$  double wells (see Fig. 1) we use the notation  $s=E, F, G, K, H$ , or  $\bar{H}$  instead.

### A. Energy levels

The computed rotationless energies  $E_k^s(v, J=0)$  were, in most cases, identified by studying each component of the corresponding multichannel total wave function [15]. In regions where diabatic vibrational level spectra from two or more electronic states are overlapping each other, comparisons with available experimental results [3,12,41] are made. Many of these levels are more or less mixed [12], making the identification difficult, or even incorrect, in terms of single characters. Levels without a clear dominating character are not given any term symbol but may be discussed with respect to their features and the regions in which they appear. Based on the rotationless energies  $E_k^s(v, J=0)$ , the corresponding rovibronic energies  $E_k^s(v, J)$ , for  $J=0, 1, \dots, 10$ , were computed for each electronic state. Let us further define the differences,  $\Delta E_k^s(v, J) = E_k^s(v+1, J) - E_k^s(v, J)$ , for rotational term sequences between two vibrational levels, and the shifts,  $\Delta E_{kk'}^s(v, J) = E_k^s(v, J) - E_{k'}^s(v, J)$  ( $k, k'=4, 5, 6; k \neq k'$ ), between approximations based on the (1-4), (1-5), and (1-6) $^1\Sigma_g^+$  manifolds.

### The $EF$ term values

The shifts,  $\Delta E_{kk'}^{EF}(v, 0)$  ( $k, k'=4, 5, 6; k \neq k'$ ), between different approximations are presented in Table II. For lower levels of the 4- and 5-state approximations  $|\Delta E_{kk'}^{EF}(0-5, 0)| < 3 \times 10^{-2} \text{ cm}^{-1}$ , i.e., within spectroscopic accuracy. For the next four levels,  $|\Delta E_{kk'}^{EF}(6-9, 0)| < 0.67 \text{ cm}^{-1}$ , which is still proportionally good. For  $v=10-32$ , all  $E_5^{EF}(v, 0)$  energies are shifted upwards relative to the  $E_4^{EF}(v, 0)$  energies. From  $v=10$  to  $20$ ,  $|E_5^{EF}(v, 0)|$  increases from  $1.34$  to  $6.93 \text{ cm}^{-1}$ . In the interval  $v=21-32$ , we found that  $|E_{45}^{EF}(v, 0)|$  is within the range  $10-35 \text{ cm}^{-1}$ , except that  $|E_{45}^{EF}(22, 0)| = 7.80 \text{ cm}^{-1}$ .

TABLE II. The  $EF$  energy differences  $\Delta E_{kk'}^{EF}(v, 0)$  ( $\text{cm}^{-1}$ ) ( $k, k'=4, 5, 6; k \neq k'$ ). Numbers in brackets denote powers of 10.

	$s$	$\Delta E_{45}^{EF}$	$\Delta E_{46}^{EF}$	$\Delta E_{56}^{EF}$
1	$E0$	2.14[-2]	-1.78[-3]	-2.31[-2]
2	$F0$	5.95[-2]	5.52[-3]	-4.29[-2]
3	$F1$	3.44[-2]	2.39[-2]	-1.06[-2]
4	$E1$	8.77[-2]	2.26[-2]	-6.51[-2]
5	$F2$	-1.15[-2]	-3.15[-2]	-2.00[-2]
6	$F3$	-2.76[-2]	-5.76[-2]	-3.00[-2]
7	$E2$	0.82	0.72	-0.10[-2]
8	$F4$	-0.44	-0.49	-5.32[-2]
9	$EF8$	-9.57[-2]	-0.18	-8.23[-2]
10	$EF9$	0.40	-0.19	-0.20
11	$EF10$	-1.07	-1.18	-0.11
12	$EF11$	-1.50	-1.60	-9.95[-2]
13	$EF12$	-1.10	-1.30	-0.20
14	$EF13$	-1.13	-1.34	-0.20
15	$EF14$	-2.07	-2.17	-0.10
16	$EF15$	-2.53	-2.63	-9.69[-2]
17	$EF17$	-1.60	-1.77	-0.19
18	$EF18$	-0.36	-0.50	-0.13
19	$EF19$	-5.83	-5.61	0.22
20	$EF20$	-2.11	-2.16	-5.78[-2]
21	$EF21$	-4.02	-4.11	-9.11[-2]
22	$EF22$	-11.87	-13.95	-2.08
23	$EF23$	-3.15	-3.70	-0.56
24	$EF24$	-11.94	-12.46	-0.52
25	$EF25$	-2.97	-2.94	3.79[-2]
26	$EF26$	-14.95	-16.38	-1.44
27	$EF27$	-16.39	-18.10	-1.71
28	$EF28$	-11.58	-11.98	-0.40
29	$EF29$	-27.08	-29.16	-2.08
30	$EF30$	-31.97	-31.62	0.35
31	$EF31$	-9.67	-10.39	-0.72
32	$EF32$	-4.06	-4.04	1.58[-2]
33	$EF33$	-9.13	-11.30	-2.18

The discrepancies  $\Delta E_{46}^{EF}(v, 0)$  in Table II show an almost identical behavior as  $\Delta E_{45}^{EF}(v, 0)$  and can be summarized as  $|\Delta E_{46}^{EF}(v, 0)| < 6 \times 10^{-2} \text{ cm}^{-1}$  for  $v=0-5$ ,  $|\Delta E_{46}^{EF}(v, 0)| \leq 0.55 \text{ cm}^{-1}$  for  $v=6-9$ , and just as in the previous case,  $E_4^{EF}(v, 0) < E_6^{EF}(v, 0)$  for  $v=10-32$ , where  $|E_{46}^{EF}(10-20, 0)|$  are within the interval  $1.46-6.86 \text{ cm}^{-1}$  and  $|E_{46}^{EF}(21-32, 0)|$  are within  $10.14-34.51 \text{ cm}^{-1}$ . An exception here is that  $|E_{46}^{EF}(22, 0)| = 8.21 \text{ cm}^{-1}$ .

According to Table II, the  $\Delta E_{56}^{EF}(v, 0)$  shifts behave differently compared to the two previous ones. For most of the levels,  $E_5^{EF}(v, 0) < E_6^{EF}(v, 0)$ , i.e., the energies are shifted upwards when adding the  $O$  state to the (1-5) $^1\Sigma_g^+$  manifold. More interesting is that  $|\Delta E_{56}^{EF}(v, 0)| \leq 0.2 \text{ cm}^{-1}$  for  $v=0-17$  and  $|\Delta E_{56}^{EF}(v, 0)| \leq 2.0 \text{ cm}^{-1}$  for  $v=18-32$ . To summa-

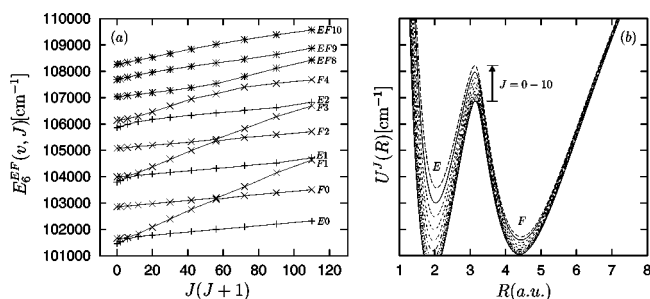


FIG. 2. (a) Rovibronic  $E_6^{EF}(v, J)$  energies as functions of  $J(J+1)$  for  $J=0-10$ ; (b) the effective potentials  $U^J(R)$  for  $J=0-10$  in the same energy region as the levels in (a).

ribe the behavior of the rotationless  $EF$  spectra we conclude that when adding the electronic  $P$  state to the  $(1-4)^1\Sigma_g^+$  manifold the energy levels, particularly for  $v \geq 10$ , are shifted. When adding the  $O$  state to the  $(1-5)^1\Sigma_g^+$  manifold most of these shifts remain unchanged. This indicates that the influence of the  $O$  state on the  $EF$  levels is almost negligible.

In Fig. 2(a) the 11 lowest  $E_6^{EF}(v, J)$  rovibronic energies are plotted as functions of  $J(J+1)$  for  $J=0-10$ . A number of avoided crossings appear in the structure of the  $E0-E1$  and  $F0-F3$  term sequences, reflecting perturbations due to the  $EF$  double-well shape. In order to achieve a deeper understanding about this level structure we can study the corresponding  $EF$  effective potentials,  $U^J(R)$ , which are displayed for  $J=0-10$  in Fig. 2(b). Thus, we are here studying low  $J$  quantum numbers for which the effective potentials are still far from being shallow. Before doing this analysis, it may be interesting to understand why the  $EF$  (and  $GK$ ) adiabatic double-well shape appears.

In a diabatic framework, the double excited configuration  $(2p\sigma_u)^2$  is allowed to cross the first excited configuration  $(1s\sigma_g)(2s\sigma_g)$  in  $H_2$ . In an adiabatic representation, the von Neumann-Wigner noncrossing rule plays an important role. Due to an interaction between these two excited configurations, two adiabatic double-well structures of  $^1\Sigma_g^+$  symmetry are formed, the  $EF$  and  $GK$  electronic states. Thus, the shape of the  $EF$  potential curve displayed in Fig. 2(b) originates from an avoided crossing situation.

According to the formula,  $U^J(R) = U^0 + J(J+1)/(2\mu R^2)$ , an effective potential generally increases as a function of the internuclear distance  $R$ . Therefore, the  $E$  effective potential wells will rise much faster than the corresponding  $F$  wells, which is clearly seen in the figure. This, together with the fact that the  $E$  well has a narrower shape than the  $F$  well, produces a larger level spacing for the  $E$  than for the  $F$  rotational energies. If we begin with the  $E0$  and  $F0$  level structures, the  $E0$  rotational energies for  $J=0-2$  are still below the corresponding  $F0$  rotational energies. For  $J=3$  the  $E0$  energy would become larger than the corresponding  $F0$  energy but, according to the noncrossing rule, an avoided intersection produces a sharp bend such that the  $E0$  term series continues along the original path of the  $F0$  term series. Similarly, the  $F0$  term series follows the original  $E0$  path. Continuing upwards along this path from  $J=3$ , we find that the rotational energy becomes larger than the  $F0$  energy for

$J=7$ . Again, this produces an avoided crossing and, consequently, the sharp bends seen in Fig. 2(b). The same reasoning can be used for the other avoided crossings appearing in the figure. The source to this specific rovibronic structure is the rather peculiar shape of the  $EF$  double-well potential.

When continuing along the paths through these avoided crossings, an essentially linear dependence is seen. This can be interpreted as if the associated rotational  $E0-E1$  and  $F0-F3$  wave functions are well localized within each of the  $E$  or  $F$  effective potential wells. Furthermore, the two rather different inclinations of this linear dependence are verified by the different shapes of the  $E$  and  $F$  wells within the corresponding effective potentials.

According to Fig. 2(a), the next term series,  $E2$ , displays an  $E$  character behavior for  $J=0-3$ , while for  $J=4-10$  the associated wave functions seem to leak out through the  $EF$  barrier into the  $F$  potential well, i.e., a situation where we have a mixture of characters. When continuing through the vibrational progression we notice that the term series assigned as  $F4$  has a somewhat bent shape, again indicating a mixing of  $E$  and  $F$  characters. The  $EF8$  series displays a slightly nonlinear dependence. Beginning with the  $J=0$  level, it lies just above the corresponding  $U^0(R)$  effective potential barrier. A similar comparison for each of the  $J=1, 2, \dots, 10$  quantum numbers shows that all rotational levels lie just above their corresponding effective  $EF$  potential barrier edge. Thus, the  $EF$  wave functions are distorted by  $E$  and/or  $F$  wave functions, causing the nonlinear shape of the  $EF8$  term series. For the  $EF9-EF10$  levels the previously discussed distortion has almost disappeared, which is reflected by the basically linear behavior in Fig. 2(a). The same analysis for the  $E_4^{EF}(v, 0-10)$  and  $E_5^{EF}(v, 0-10)$  rovibronic term values displayed almost identical patterns as  $E_6^{EF}(v, 0-10)$ .

In the higher  $EF$  spectra, between  $EF10$  and  $K0$ , perturbations should be absent or weak. This was verified by plotting the corresponding  $E_k^{EF}(v, 0-10)$  ( $k=4, 5, 6$ ) levels for  $v=11-18$ , not displayed here. All these rovibronic levels are still below the  $GK$  spectra, and each of the three sets of term series display a strictly linear structure.

The upper part of the  $EF$  spectra contains vibrational levels which appear in an overlapping region, including both  $GK$  and  $H$  levels as well. This implies that perturbations may occur between levels of different characters. Figure 3 shows a number of  $EF$  energy results originating from calculations using the  $(1-6)^1\Sigma_g^+$  manifold. Here, we have entered a region where the  $EF$ ,  $GK$ , and  $H$  spectra are overlapping each other. The linear dependence is clearly broken for a number of term series, indicating homogeneous perturbations caused by the  $GK$  and/or the  $H$  spectra.

The  $EF23$  term series is essentially linear up to  $J=6$ , but for  $J=7-10$  the rotational energies are pushed upwards according to the bent shape seen in Fig. 3. This is most likely due to a perturbation from the  $GK$  spectrum displayed in Fig. 4. The  $GK3$  term series lies in the same energy region as the  $EF23$  rotational levels, and its linear behavior is broken for  $J=6$ . The  $J=7-10$  rotational energies are pushed downwards, indicating a repulsion from the  $EF23$  series.

The  $H0-H2$  levels are assumed to give only a weak perturbation contribution here. This will be further discussed in

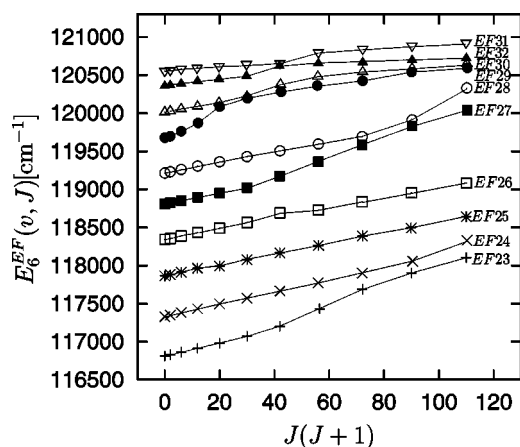


FIG. 3. Rovibronic  $E_6^{EF}(v, 23-32, J)$  energies as functions of  $J(J+1)$  for  $J=0-10$ .

a subsequent section. The situation may be better understood by inspecting the potential-energy curves displayed in Fig. 1. While the  $H$  potential has a smooth shape in the energy region of interest, the  $GK$  potential well changes drastically in the sense that it goes from a double-well ( $G$  and  $K$ ) to a single-well ( $GK$ ) shape. The next three term series,  $EF24$ – $EF26$ , do not show considerable signs of perturbations. According to Fig. 3, the  $EF27$  and  $EF28$  rotational spectra display an avoided crossing between  $J=8$  and  $9$ . According to their shapes, these two term series are obviously perturbed, particularly the  $EF27$  rotational levels. This conclusion is further supported by the study of Yu and Dressler [12], where they reported an  $EF(88\%)$  and  $GK(12\%)$  mixture for the  $EF27$  character. By comparing the  $EF$  and  $GK$  spectra we find that the  $GK5$  rotational energies, which lies in the same energy region as the  $EF27$  rotational spectra, are pushed downwards.

The  $GK5$  rotational spectra is probably not the only reason for the spectroscopic perturbation seen in the  $EF27$  rotational energies. Figure 5 indicates that the  $H2$  rotational spectra also may contribute to the spectroscopic perturbation of the  $EF27$  term series. The  $EF29$ – $EF32$  rotational spectrum is rather dense and is further superimposed onto the

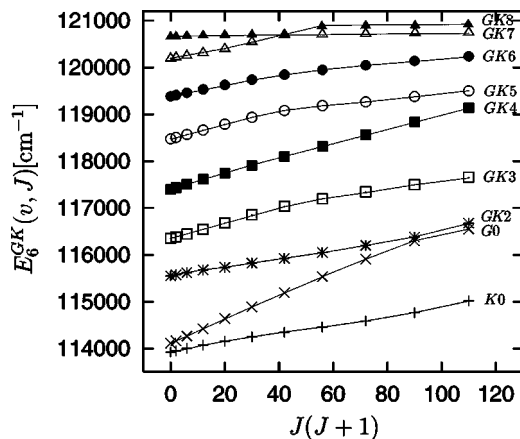


FIG. 4. Rovibronic  $E_6^{GK}(v, J)$  energies as functions of  $J(J+1)$  for  $J=0-10$ .

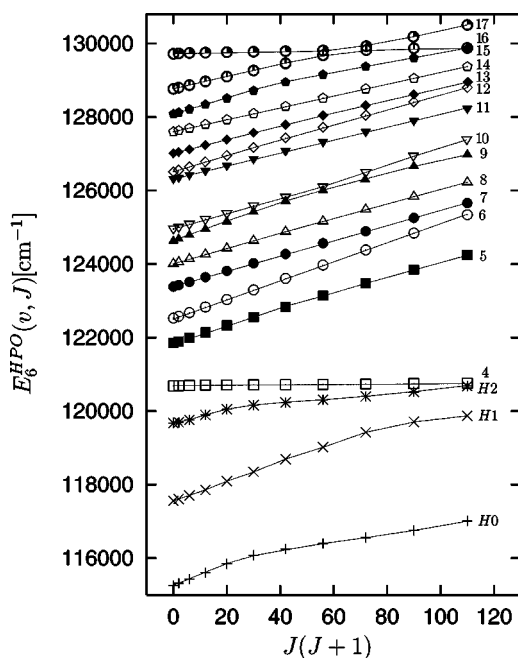


FIG. 5. Rovibronic  $E_6^{HPO}(v, J)$  energies as functions of  $J(J+1)$  for  $J=0-10$ . The three lowest levels are assigned as  $H0$ ,  $H1$ , and  $H2$ . All higher term series may be of  $H$ ,  $P$ , and/or  $O$  characters, but these levels are not identified for certain.

$GK7$ – $GK8$  and  $H2$  rotational spectra. This was also pointed out by Yu and Dressler [12], and by comparing their plot of rovibronic term values (Fig. 2, upper part) we find a similar behavior for our  $EF29$ – $EF30$  results as they reported. They found avoided crossings for term series of different vibronic states. This is the repulsive behavior of the different  $EF$  term series discussed above. The almost horizontal dependence of the  $EF31$  and  $EF32$  term series indicate a continuum-bound-state behavior which is explained by the fact that the  $EF$  threshold ( $\sim 120\,700\text{ cm}^{-1}$ ) has been reached.

## 2. The $GK$ levels

Our  $E_k^{GK}(v, 0)$  results are presented in Table III. When comparing the rotationless levels in the 4- and 5-state approximations, all 5-state vibrational levels are shifted upwards relative to the 4-state levels. These shifts,  $|\Delta E_{45}(v, 0)|$ , are all between  $5.4\text{ cm}^{-1}$  (for  $v=10$ ) and  $46.3\text{ cm}^{-1}$  (for  $v=6$ ). The corresponding  $|\Delta E_{46}(v, 0)|$  shifts show a similar behavior and are in the interval  $5.8$ – $48.7\text{ cm}^{-1}$ .  $|\Delta E_{56}(v, 0)|$  are still shifted upwards but are much smaller than the previous ones. Here  $|\Delta E_{56}(v, 0)|$  are in the interval  $0.21$ – $5.4\text{ cm}^{-1}$ . Although  $|\Delta E_{56}(v, 0)| > 5\text{ cm}^{-1}$  for one level they are generally less than  $3\text{ cm}^{-1}$ . Due to the results of these comparisons, the effect of adding the  $P$  state to the  $(1-4)^1\Sigma_g^+$  manifold is much stronger than when adding the  $O$  state to the  $(1-5)^1\Sigma_g^+$  system.

Figure 4 shows the  $J(J+1)$  behavior of  $GK$  rovibronic energies. As was pointed out in the preceding section, all  $GK$  levels are in a region where both  $EF$  and  $H$  levels appear as well. The  $K0$  and  $G0$  levels are well localized within each of the  $G$  and  $K$  potentials, and therefore show an essentially

TABLE III. The  $GK$  energy differences  $\Delta E_{kk'}^s(v,0)$  ( $k,k'=4,5,6; k \neq k'; s=H,GK$ ) between the 4-, 5-, and 6-state approximations.

	$s$	$\Delta E_{45}^s$	$\Delta E_{46}^s$	$\Delta E_{56}^s$
1	$K0$	-13.76	-13.77	7.96[-3]
2	$G0$	-5.90	-6.16	-0.26
3	$H0$	1.22	1.78	0.56
4	$GK2$	-17.09	-20.47	-3.38
5	$GK3$	-24.07	-24.98	-0.91
6	$GK4$	-33.78	-39.94	-6.15
7	$H1$	6.66	6.36	-0.30
8	$GK5$	-25.38	-26.47	-1.10
9	$GK6$	-42.57	-43.46	-0.89
10	$H2$	-13.42	-13.77	-0.35
11	$GK7$	-16.90	-17.87	-0.97
12	$GK8$	-10.91	-14.00	-3.07

linear behavior. The  $GK2$  and  $GK4$  term series also seem to be more or less unperturbed according to the plot. The rest of the  $GK$  rovibronic level dependence is not linear over the  $J=0-10$  interval. For the  $GK3$  and  $GK5-GK6$  rotational structure we refer to the previous discussion about the  $EF$  spectra as the homogeneous perturbations discussed there are mutual. The  $GK7-GK8$  term sequences behave as the  $EF31-EF32$  levels and can, similarly, be explained by the  $GK$  energy threshold.

### 3. The $H$ , $P$ , and $O$ levels

When the  $(1-6)^1\Sigma_g^+$  manifold was used in our calculations a total number of 17 vibrational  $H$ ,  $P$ , and  $O$  levels were found in the energy region  $(115\,000-131\,000)$   $\text{cm}^{-1}$ . The  $E_6^H(0-2,0)$  levels are easily identified as they are essentially unshifted when compared with the corresponding  $(1-4)$  and  $(1-5)^1\Sigma_g^+$  results. The identification of the other  $H$ ,  $P$ ,  $O$  rotationless levels in this interval is more uncertain. When comparing results based on calculations for the  $(1-4)$  and  $(1-5)^1\Sigma_g^+$  manifolds, the  $H$  levels above  $H2$  are seen to be considerably shifted. Thus, the  $H$  energy-level positions, computed with the  $(1-4)^1\Sigma_g^+$  manifold, cannot be used in the identification of the  $H$  and  $P$  spectra obtained with the  $(1-5)^1\Sigma_g^+$  states. When adding the  $O$  electronic state to the  $(1-5)^1\Sigma_g^+$  manifold, the calculated spectra again change their structure. This makes the analysis even more difficult.

A study of the rovibronic spectra often gives some additional information. In Fig. 5 our computed  $E_6^{HPO}(v,J)$  rovibronic term series for  $J=0-10$ , in the energy region  $115\,000-131\,000$   $\text{cm}^{-1}$ , are displayed. The nonlinear behavior of the  $H0-H2$  term series indicates spectroscopic perturbations. This is most likely because of a strong mixing of electronic states as these levels are within a region where both  $EF$  and  $GK$  levels appear as well. This level mixing has been reported in the theoretical study by Yu and Dressler [12] where they graphically presented a number of rovibronic term sequences. In their Fig. 2, the  $H2$  rotational en-

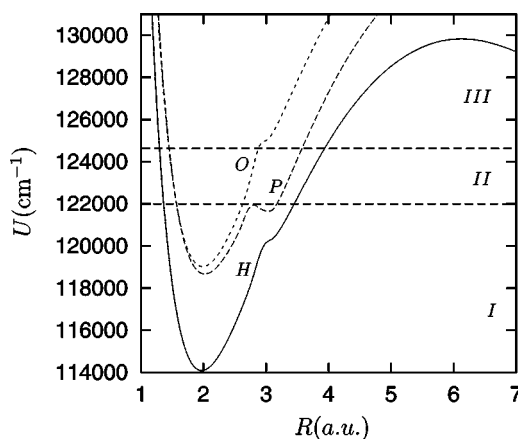


FIG. 6. The best adiabatic  $H$ ,  $P$ , and  $O$  potential-energy curves in a chosen energy region.

ergies are displayed as functions of  $J(J+1)$  for  $J=0-5$ . The shape of this plot agrees with our curve displayed in Fig. 5. As was pointed out by Yu and Dressler [12], the choice of term symbols may be somewhat arbitrary for such strongly mixed states as we have here.

The fourth rovibronic term series (squares) from below, in Fig. 5, follows an essentially horizontal line. This may be explained by the fact that its rovibronic energy interval  $120\,686-120\,757$   $\text{cm}^{-1}$  for  $J=0-10$  lies just at the  $EF$  and  $GK$  dissociation limits ( $\sim 120\,700$   $\text{cm}^{-1}$ ). Similar behavior is seen for the highest term sequence (“quarter filled circles”) in Fig. 5. The reason for this might be that the corresponding energy interval  $129\,721-129\,877$   $\text{cm}^{-1}$  is centered around the  $H\bar{H}$  local potential maximum ( $129\,825$   $\text{cm}^{-1}$ ).

Most of the other 12 rovibronic sequences presented in Fig. 5 follow essentially straight lines, indicating that they are unperturbed or only weakly perturbed. Although different inclinations appear in this linear structure, the identification of the corresponding characters is relatively uncertain. However, a good guess may be based on the following arguments: Consider the chosen parts of the best adiabatic  $H$ ,  $P$ , and  $O$  potential-energy curves displayed in Fig. 6. According to the shapes and widths of these potentials, the  $H$  vibrational energies should generally have a smaller level spacing than the  $P$  and  $O$  states in the same energy region. Thus, the vibrational energy spacing of the  $O$  levels should be somewhat greater than for the  $P$  levels. Consequently, when considering each of the  $H$ ,  $P$ , and  $O$  term sequences, they should have somewhat different inclinations. Unfortunately, due to the shape of the three potentials, these inclinations vary within each of the  $H$ ,  $P$ , and  $O$  rovibronic spectra, making the identification rather difficult.

There are essentially three different intervals to consider here. The first (I) is between  $114\,000$  and  $120\,000$   $\text{cm}^{-1}$ , the second (II) is between  $122\,200$  and  $124\,500$   $\text{cm}^{-1}$ , and the third (III) is between  $124\,500$  and the  $H$  threshold at about  $129\,825$   $\text{cm}^{-1}$ . When going from region I to II the potentials get wider, particularly the  $P$  and  $O$  wells. Because of this, the corresponding vibrational energy-level spacings and the local rotational constants, defined as

$$B_{v,J} = \left\langle \chi_{v,J}^{(d)}(R) \left| \frac{1}{R^2} \right| \chi_{v,J}^{(d)}(R) \right\rangle, \quad (39)$$

decrease. The  $B_{v,J}$  constant is a measure of the  $1/R^2$  distribution of the diabatic wave functions  $\chi_{v,J}^{(d)}(R)$ , and thus tells us in what internuclear distance region the dominating level wave function is located. According to Carlsund-Levin *et al.* [14], an estimate of the local  $B_{v,J}$  value can be obtained as the slope of the term energy series as a function of  $J(J+1)$ .<sup>1</sup> However, we can still compare the inclinations of the  $H$ ,  $P$ , and  $O$  rovibronic term sequences within each interval. In region II, we have three parallel term series, having a similar inclination as the  $H1$  and  $H2$  term series. The corresponding vibrational energy-level spacings suggest that the term series 5, 7, and 10 in Fig. 5 are  $H$  rovibronic energies. The term series denoted as 8 in the figure has essentially the same inclination and is therefore most likely of a  $P$  character. This is further supported by the fact that the  $H$  and  $P$  potential shapes and widths are quite similar in region II. The remaining rovibronic levels, 6 and 9, are finally interpreted as  $O$  electronic term values. Continuing to interval III, and using the same arguments as for the previous regions, we interpret levels 11, 14, and 16 as  $H$  term series. This makes a total number of nine  $H$  levels, which is in agreement with the number of  $H$  vibrational levels found when the  $(1-4)^1\Sigma_g^+$  manifold was used in our calculations. The rovibronic sequence 12 is probably of an  $O$  character, while 13 then should be a  $P$  term series. The linear behavior is clearly broken for series 15 and it might therefore be of a mixed  $P$  and  $O$  character. The highest term sequence (17) lies at the  $H$  threshold which is reflected by the horizontal linear dependence.

Above the  $H$  threshold we have to distinguish between the  $H\bar{H}$ ,  $P$ , and  $O$  spectra. However, according to our previous discussion about the influence of different potential shapes on the rovibronic term energies, the  $H\bar{H}$  spectrum is easily identified. This will be further discussed below. Thus, the remaining levels in the same energy region are of  $P$  or  $O$  characters. A general conclusion from an inspection of Fig. 7 is that there exist only weak spectroscopic perturbations in this energy region.

By comparing the rovibronic  $(1-5)^1\Sigma_g^+$  results presented in Fig. 7(a), where the  $O$  electronic state is excluded, with the  $(1-6)^1\Sigma_g^+$  results presented in Fig 7(b), we were able to sort out seven probable  $P$  levels. However, according to the plot, there are a number of avoided crossings, indicating that some of these  $P$  levels are perturbed by the  $O$  rovibronic spectra. The rest of the term series, appearing only in the  $(1-6)^1\Sigma_g^+$  spectra, should be of an  $O$ , or perhaps of a mixed  $P$  and  $O$ , character. This is supported by the fact that these term sequences have a steeper inclination than the others for lower  $J$  values. This is further in agreement with the more narrow shape of the  $O$  potential than for the  $P$  well within the same energy interval. The highest identified  $P$  term series

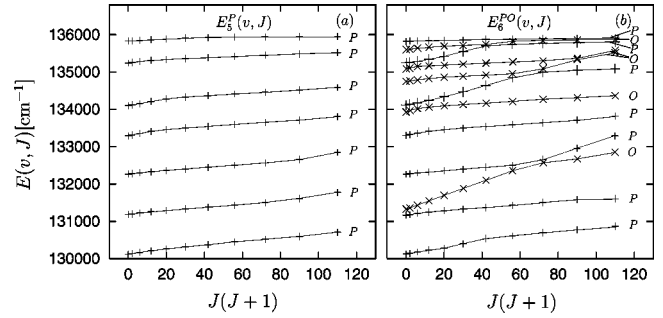


FIG. 7. Rovibronic term sequences as functions of  $J(J+1)$  in the interval 130 000–136 800  $\text{cm}^{-1}$  for (a)  $E_5^P(v, J)$  and (b)  $E_6^{PO}(v, J)$  energies for  $J=0-10$ .

135 820–135 909  $\text{cm}^{-1}$ , close to the dissociation limit, shows an almost horizontal behavior. This is also the case for the rotational energies of the highest  $O$  level as well as for the second highest  $P$  rotational levels for  $J > 5$ . Two of the term series (4 and 5 from above) were identified as having an  $O$  character, although they seem to be too close to each other. An alternative is that one of these term series (5 from above) is of a  $P$  character. It is likely, according to Fig. 7(a), that the energy gap between the 5th and 6th term series is considerably larger than the previous gap between the 4th and 5th term series. Thus, somewhere at about 134 700–134 800  $\text{cm}^{-1}$ , a possibly existing term series could be missing.

#### 4. The $\bar{H}$ levels

The computed  $\bar{H}0-H15$  levels most likely have well localized wave functions within the  $\bar{H}$  potential well, because its minimum is at  $R \approx 10$  a.u., i.e., more or less isolated from the other electronic states which have their potential minima within the interval  $R=2-4$  a.u. This is clearly verified when comparing the different approximations studied here. According to Table IV,  $|\Delta E_{45}^{\bar{H}}(v, 0)| < 9.8 \times 10^{-2} \text{ cm}^{-1}$  for  $v=0-9$ , and  $|\Delta E_{45}^{\bar{H}}(v, 0)| \leq 0.35 \text{ cm}^{-1}$  for  $v=10-14$ , and  $|\Delta E_{45}^{\bar{H}}(15, J=0)| < 1.15 \text{ cm}^{-1}$ , i.e., a good agreement between most of the energies for the 4- and 5-state approximations.

A similar pattern was seen for  $\Delta E_{46}^{\bar{H}}(v, 0)$  and  $\Delta E_{56}^{\bar{H}}(v, 0)$ . This can be summarized as  $|\Delta E_{46}^{\bar{H}}(v, 0)| \leq 8.4 \times 10^{-2} \text{ cm}^{-1}$  for  $v=0-7$ ,  $|\Delta E_{46}^{\bar{H}}(v, 0)| \leq 0.45 \text{ cm}^{-1}$  for  $v=8-14$ ,  $\Delta E_{46}^{\bar{H}}(15, 0) = 25.3 \text{ cm}^{-1}$ ,  $|\Delta E_{56}^{\bar{H}}(v, 0)| < 8.65 \times 10^{-2} \text{ cm}^{-1}$  for  $v=0-13$ ,  $|\Delta E_{56}^{\bar{H}}(14, 0)| = 0.12 \text{ cm}^{-1}$ , and  $|\Delta E_{56}^{\bar{H}}(15, 0)| = 24.11 \text{ cm}^{-1}$ . According to Table IV all  $E_5^{\bar{H}}(0-14, 0)$  and  $E_6^{\bar{H}}(0-14, 0)$  levels are shifted upwards when compared to the  $E_4^{\bar{H}}(0-14, 0)$  levels. The same is true for the  $E_6^{\bar{H}}(0-14, 0)$  levels when compared to the  $E_5^{\bar{H}}(0-14, 0)$  levels, but the shifts are much less than in the previous case. The rotationless  $v=15$  energy level is shifted downwards by about 24  $\text{cm}^{-1}$  when the  $P$  electronic state is included in the calculations, while it remains more or less the same when the  $O$  electronic state is included. Thus, it seems to be the  $P$  electronic state that affects the  $\bar{H}$  energy-level spectra the most.

<sup>1</sup>The definition of Carlsund-Levin *et al.* [14] was based on Hund's case-(b) type interactions, i.e., the  $N$  quantum number was used instead of  $J$ .

TABLE IV. The  $\bar{H}$  energy differences  $\Delta E_{kk'}^{\bar{H}}(v,0)$  ( $k,k'=4,5,6;k \neq k'$ ) between the 4-, 5-, and 6-state approximations.

$s$		$\Delta E_{45}^{\bar{H}}$	$\Delta E_{46}^{\bar{H}}$	$\Delta E_{56}^{\bar{H}}$
1	$\bar{H}0$	-1.52[-2]	-1.53[-2]	-1.41[-4]
2	$\bar{H}1$	-1.93[-2]	-2.08[-2]	-1.56[-3]
3	$\bar{H}2$	-2.59[-2]	-2.79[-2]	-2.01[-3]
4	$\bar{H}3$	-3.21[-2]	-3.57[-2]	-3.64[-3]
5	$\bar{H}4$	-3.96[-2]	-4.47[-2]	-5.10[-3]
6	$\bar{H}5$	-4.87[-2]	-5.63[-2]	-7.51[-3]
7	$\bar{H}6$	-5.88[-2]	-6.86[-2]	-9.80[-3]
8	$\bar{H}7$	-6.97[-2]	-8.38[-2]	-1.40[-2]
9	$\bar{H}8$	-8.27[-2]	-0.10	-1.92[-2]
10	$\bar{H}9$	-9.78[-2]	-0.12	-2.67[-2]
11	$\bar{H}10$	-0.12	-0.15	-3.64[-2]
12	$\bar{H}11$	-0.14	-0.19	-4.91[-2]
13	$\bar{H}12$	-0.16	-0.22	-6.36[-2]
14	$\bar{H}13$	-0.35	-0.44	-8.64[-2]
15	$\bar{H}14$	-0.17	-0.28	-0.12
16	$\bar{H}15$	-1.15	25.25	24.11

The rovibronic  $E_6^{\bar{H}}(0-15,J)$  term values for  $J=0-10$  are displayed in Fig. 8. The curves  $\bar{H}0-\bar{H}14$  do not show any signs of perturbations. Only the  $\bar{H}15$  term series behaves a little differently but still not as if it was perturbed by another state. The  $J=0$  energy is positioned at an expected vibrational spacing but for  $J>0$  interactions with the  $H\bar{H}$  continuum occur as indicated by the plot.

### 5. The $H\bar{H}$ levels

Our computed rotationless  $E_k^{H\bar{H}}(v,0)$  ( $k=4,5,6$ ) energy levels, i.e.,  $H\bar{H}$  vibrational energies above the  $H$  and  $\bar{H}$  spec-

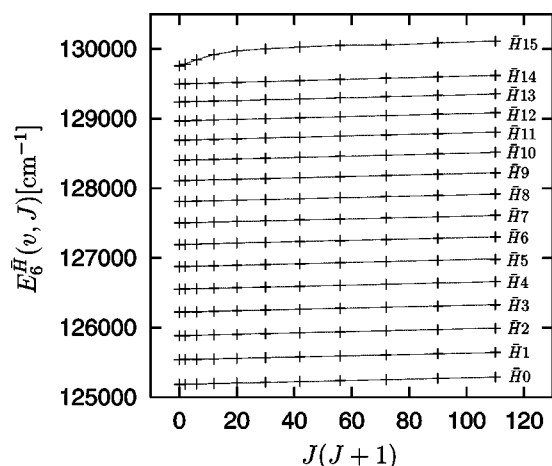


FIG. 8. Rovibronic  $E_6^{\bar{H}}(v=0-15,J)$  energies as functions of  $J(J+1)$  for  $J=0-10$ .

tra, are not presented graphically here. The reason is that the  $H\bar{H}$  spectra do not show significant signs of perturbations even if some internal shifts were found for the different approximations. The rotationless energy results are presented in Table V, where the lowest level is denoted as  $H\bar{H}25$ . This choice of numbering is based on the fact that the  $H$  and  $\bar{H}$  spectra below the lowest  $H\bar{H}$  level, i.e.,  $H0-H8$  and  $\bar{H}0-\bar{H}15$ , makes 25 levels in total (see previous sections). To summarize the differences in the rotationless level structures 4-, 5-, and 6-state approximations we found that  $|\Delta E_{45}^{H\bar{H}}(v,0)|$  varies within  $0.6-89.5$   $\text{cm}^{-1}$ ,  $|\Delta E_{46}^{H\bar{H}}(v,0)|$  within  $0.2-89.5$   $\text{cm}^{-1}$ , and  $|\Delta E_{56}^{H\bar{H}}(v,J=0)|$  within  $0.2-91.3$   $\text{cm}^{-1}$ . The variations within these intervals are rather different when comparing the three approximations with each other. We computed levels for  $v=0-32$  but whether the higher of these levels should be considered as isolated resonances or overlapping resonances is a matter of definition.

The rovibronic energies  $E_k^{H\bar{H}}(v,J)$  for  $J=0-10$  ( $k=4,5,6$ ) were also studied as functions of  $J(J+1)$ . These three structures were found to behave essentially linearly. Only for a few higher levels this linearity was slightly broken, indicating possible perturbations originating from the  $P$  and/or  $O$  electronic states.

### B. Level widths

All computed rotationless level widths  $\Gamma_k^s(v,0)$  are reported in Tables VI-VIII. In the case of rovibronic level widths  $\Gamma_k^s(v,J)$  strong variations within a vibrational level may indicate electronic spectroscopic perturbations [15]. It is important to emphasize that this is particularly useful within a relatively limited interval of the  $J$  quantum number. For high rotational levels the corresponding effective potentials become more and more shallow. This, in turn, generally implies stronger and stronger predissociation until the continuum is reached. In general, for higher vibrational levels approaching the threshold, this situation occurs for much lower rotational levels than for lower vibrational levels. Within the interval  $J=0-10$  most of the level widths, except a few at the thresholds, are still relatively narrow. Furthermore, the inclination of the rotational level widths within a vibronic level may be positive, horizontal, or negative. That is, the widths are either increasing, staying constant, or decreasing. However, what is relevant for the perturbation studies here are mainly signs of nonlinearity, irrespective of the inclination of the rotational dependence of the widths.

According to Figs. 9-11,  $\log_{10}\Gamma_k^s(v,J)$  was plotted as functions of  $J(J+1)$  for  $J=0-10$ . The choice of using a logarithmic scale is because the widths are often varying with several orders of magnitude, making a graphical representation in a linear scale inconvenient.

#### 1. The $EF$ widths

Our calculated rotationless level widths  $\Gamma_k^{EF}(v,0)$  ( $k=4,5,6$ ) are presented in Table VI. Most of the lower widths are within  $10^{-11}-10^{-6}$   $\text{cm}^{-1}$ , while for higher levels they are

TABLE V. The  $H\bar{H}$  vibrational level spacing,  $\Delta E_k^{H\bar{H}}(v,0)$  ( $\text{cm}^{-1}$ ), and energy differences,  $\Delta E_{kk'}^{H\bar{H}}(v,0)$  ( $\text{cm}^{-1}$ ) ( $k, k'=4,5,6; k \neq k'$ ), between the 4-, 5-, and 6-state approximations.

	$s$	$\Delta E_4^{H\bar{H}}$	$\Delta E_5^{H\bar{H}}$	$\Delta E_6^{H\bar{H}}$	$\Delta E_{45}^{H\bar{H}}$	$\Delta E_{46}^{H\bar{H}}$	$\Delta E_{56}^{H\bar{H}}$
1	$H\bar{H}25$	0	0	0	-15.19	23.74	38.92
2	$H\bar{H}26$	145.18	134.95	103.23	-25.41	-18.21	7.20
3	$H\bar{H}27$	206.31	273.06	266.77	41.33	42.24	0.91
4	$H\bar{H}28$	194.93	183.30	179.35	29.71	26.66	-3.05
5	$H\bar{H}29$	193.04	182.67	180.59	19.34	14.21	-5.13
6	$H\bar{H}30$	200.51	190.29	189.66	9.11	3.35	-5.76
7	$H\bar{H}31$	205.62	195.92	193.39	-0.60	-8.88	-8.28
8	$H\bar{H}32$	207.88	297.40	287.74	88.93	70.98	-17.95
9	$H\bar{H}33$	208.95	155.31	170.70	35.29	32.73	-2.56
10	$H\bar{H}34$	210.25	189.39	187.40	14.43	9.88	-4.54
11	$H\bar{H}35$	212.99	203.96	203.35	5.39	0.24	-5.15
12	$H\bar{H}36$	217.26	210.93	210.26	-0.94	-6.76	-5.82
13	$H\bar{H}37$	221.34	299.63	317.59	77.35	89.49	12.14
14	$H\bar{H}38$	223.95	160.03	148.10	13.43	13.64	0.21
15	$H\bar{H}39$	225.26	217.41	210.59	5.58	-1.02	-6.61
16	$H\bar{H}40$	224.20	224.03	218.15	5.41	-7.08	-12.49
17	$H\bar{H}41$	221.20	221.33	215.49	5.55	-12.79	-18.33
18	$H\bar{H}42$	219.04	239.23	238.02	25.74	6.19	-19.55
19	$H\bar{H}43$	216.89	216.38	205.35	25.23	-5.35	-30.57
20	$H\bar{H}44$	213.23	218.67	208.90	30.66	-9.68	-40.34
21	$H\bar{H}45$	207.49	209.44	212.33	32.61	-4.84	-37.45
22	$H\bar{H}46$	202.71	219.74	203.36	49.64	-4.19	-53.83
23	$H\bar{H}47$	197.15	203.27	193.90	55.76	-7.44	-63.20
24	$H\bar{H}48$	189.16	200.05	187.21	66.65	-9.39	-76.04
25	$H\bar{H}49$	182.17	38.07	189.87	-77.46	-1.69	75.77
26	$H\bar{H}50$	172.28	328.79	166.52	79.05	-7.45	-86.50
27	$H\bar{H}51$	162.69	173.17	168.40	89.53	-1.73	-91.27
28	$H\bar{H}52$	150.66		149.36		-3.04	
29	$H\bar{H}53$	138.42	152.58	136.52	-46.97	-4.94	42.03
30	$H\bar{H}54$	123.85	209.94	123.61	39.12	-5.18	-44.30
31	$H\bar{H}55$	108.19		110.62		-2.75	
32	$H\bar{H}56$	90.84	224.05	91.12	64.14	-2.46	-66.60
33	$H\bar{H}57$	71.23		75.75		2.05	

generally found to be of the order of  $10^{-6}$ – $10^{-4}$   $\text{cm}^{-1}$ . Thus, most of the  $EF$  levels have rather narrow widths, indicating a weak predissociation. This is, at least qualitatively, in agreement with the study of Quadrelli *et al.* [2]. Furthermore, some differences are seen for the three approximations. With a few exceptions, it is generally found that  $\Gamma_5^{EF}(v,0) < \Gamma_4^{EF}(v,0) < \Gamma_6^{EF}(v,0)$ . In the analysis of the  $EF$  energies we concluded that a number of levels were more or less perturbed. In order to further investigate this we studied

the rotational dependence of  $\log_{10}\Gamma_6^{EF}(v,J)$  for  $J=0$ – $10$ .

In Fig. 9(a) the logarithm of the  $E0$ – $EF8$  series of level widths is plotted as functions of  $J(J+1)$ . The avoided crossings, appearing in the  $E0$ – $E2$  and  $F0$ – $F3$  rovibronic energy structure displayed in Fig. 2(a), are here reflected by the sudden jumps in the corresponding widths. As an example, we consider the  $E0$  width, which suddenly decreases from  $5 \times 10^{-6}$  to about  $10^{-9}$   $\text{cm}^{-1}$  when going from  $J=2$  to 3. This is due to the previously discussed avoided crossing between

TABLE VI. The  $EF$  energy shift differences  $\delta E_{c-o}^{EF}(v,0)$  ( $\text{cm}^{-1}$ ) between the present and observed levels from Ref. [12], the corresponding present widths  $\Gamma_k^{EF}(v,0)$  ( $\text{cm}^{-1}$ ) ( $k=4,5,6$ ), and the theoretical widths  $\Gamma_0^{EF}(v,0)$  ( $\text{cm}^{-1}$ ) from Ref. [11].

	$s$	$\delta E_{c-o}^{EF}$	$\Gamma_4^{EF}$	$\Gamma_5^{EF}$	$\Gamma_6^{EF}$	$\Gamma_a^{EF}$
1	$E0$	0	2.98[-7]	2.11[-8]	3.79[-6]	1.5[-11]
2	$F0$	0.61	8.95[-11]	4.52[-9]	4.62[-9]	8.6[-11]
3	$F1$	0.01	3.36[-10]	1.66[-8]	1.51[-8]	9.2[-10]
4	$E1$	-0.27	1.43[-7]	2.21[-7]	2.85[-5]	2.0[-7]
5	$F2$	0.35	4.55[-8]	1.37[-7]	2.07[-8]	9.1[-10]
6	$F3$	-0.50	2.84[-7]	4.61[-7]	7.20[-8]	3.4[-10]
7	$E2$	0.27	8.95[-6]	4.67[-7]	7.92[-5]	2.1[-8]
8	$F4$	0.63	9.16[-7]	2.11[-6]	3.21[-5]	6.0[-9]
9	$EF8$	-2.22	1.27[-6]	3.23[-6]	4.01[-5]	2.1[-8]
10	$EF9$	1.75	1.32[-5]	5.36[-6]	1.62[-4]	1.7[-7]
11	$EF10$	2.97	1.57[-5]	1.20[-6]	1.40[-4]	1.8[-7]
12	$EF11$	-1.43	1.30[-5]	1.59[-8]	1.33[-4]	1.2[-7]
13	$EF12$	0.45	1.45[-5]	1.93[-8]	2.21[-4]	2.9[-8]
14	$EF13$	1.88	1.51[-5]	6.63[-9]	3.06[-4]	3.4[-8]
15	$EF14$	0.44	1.81[-5]	6.17[-8]	3.71[-4]	3.2[-7]
16	$EF15$	-0.39	3.36[-5]	1.30[-6]	5.25[-4]	6.8[-7]
17	$EF16$	0.56	7.17[-5]	5.58[-6]	7.98[-4]	6.9[-7]
18	$EF17$	1.69	1.19[-4]	1.21[-5]	9.80[-4]	1.5[-7]
19	$EF18$	-5.75	8.56[-5]	7.22[-6]	3.84[-4]	6.4[-7]
20	$EF19$	5.30	1.95[-4]	2.94[-5]	1.65[-3]	1.9[-10]
21	$EF20$		1.94[-4]	5.54[-5]	1.45[-3]	7.5[-7]
22	$EF21$		1.17[-4]	7.18[-5]	2.43[-3]	1.5[-7]
23	$EF22$		2.31[-4]	1.33[-5]	2.12[-3]	2.4[-8]
24	$EF23$		1.77[-4]	4.32[-5]	2.21[-3]	5.4[-6]
25	$EF24$	1.05	2.31[-4]	4.45[-5]	3.57[-3]	9.2[-7]
26	$EF25$	-4.62	1.86[-4]	9.89[-6]	1.93[-3]	1.0[-5]
27	$EF26$	3.71	1.80[-4]	6.56[-7]	1.34[-3]	7.9[-6]
28	$EF27$	2.40	1.79[-4]	1.55[-6]	2.54[-3]	4.2[-6]
29	$EF28$		9.10[-5]	3.07[-5]	5.45[-4]	1.6[-6]
30	$EF29$		3.23[-5]	1.27[-5]	2.53[-3]	1.7[-6]
31	$EF30$		7.42[-5]	1.41[-6]	1.25[-3]	9.5[-7]
32	$EF31$		1.75[-4]	1.30[-5]	3.33[-3]	7.4[-8]
33	$EF32$	-9.18	4.22[-5]	1.43[-6]	9.51[-4]	3.5[-6]

the  $E0$  and  $F0$  term series. At the same point, the  $F0$  width makes a jump of the same order of magnitude in the other direction. Between  $J=3$  and 10, the  $E0$  width varies more smoothly, having a local minimum of about  $10^{-10} \text{ cm}^{-1}$  for  $J=5-6$ .

The variation of the width is about two orders of magnitude within the interval  $J=3-10$ . The reasons for this may be manifold, but an investigation of the effective potentials displayed in Fig 2(b) might give us some further information. According to the theory of quantum-mechanical tunneling, the smaller the area of the cutoff hill, and the greater the frequency of the vibration, the shorter the mean lifetime of the level [42]. If we assume that this area here becomes smaller as a function of the distance from the level to the barrier edge, the probability for penetration to a neighboring

well varies with the height of the effective barrier when counted from the corresponding rotational level. Between  $J=3$  and 6, the  $E$  effective potential minimum approaches the corresponding  $F$  potential minimum. Somewhere between  $J=5$  and 6 the minimum of the  $E$  potential passes the corresponding  $F$  minimum. From that point the effective barrier height as well as the cutoff hill area becomes smaller and smaller, implying higher penetration probabilities, i.e., the level will have more of a  $F$  character and thus a larger width.

The behavior of the other  $E$  and  $F$  rovibronic widths may be qualitatively explained in a similar way. Furthermore, the general behavior of the level widths, in the region where avoided crossings appear, is that they vary linearly, or slightly nonlinearly, within each interval between the avoided crossings. Note that intervals displaying somewhat

TABLE VII. The  $GK$  and  $H$  energy shift differences  $\delta E_{c-o}^s(v, 0)$  ( $\text{cm}^{-1}$ ) ( $k=4, 5, 6; s=GK, H$ ) between the present and the observed levels reported in Ref. [12], the corresponding present widths  $\Gamma_k^s(v, 0)$  ( $\text{cm}^{-1}$ ) ( $k=4, 5, 6; s=GK, H$ ), and the theoretical widths  $\Gamma_a^s(v, 0)$  ( $\text{cm}^{-1}$ ) ( $s=GK, H$ ) from Ref. [11].

	$s$	$\delta E_{c-o}^s$	$\Gamma_4^s$	$\Gamma_5^s$	$\Gamma_6^s$	$\Gamma_a^s$
1	$K0$	0	4.15[-5]	1.48[-2]	7.94[-4]	1.8[-4]
2	$G0$	18.67	8.09[-6]	2.41[-3]	8.56[-5]	1.6[-6]
3	$H0$	0	6.91[-7]	1.20[-4]	8.94[-6]	3.5[-7]
4	$GK2$		8.84[-5]	2.99[-3]	9.24[-5]	2.7[-6]
5	$GK3$	12.32	1.97[-6]	1.67[-3]	1.65[-4]	5.3[-6]
6	$GK4$		5.20[-7]	5.22[-3]	2.75[-4]	1.8[-5]
7	$H1$	21.48	1.12[-8]	1.58[-6]	2.47[-4]	1.6[-6]
8	$GK5$	-4.43	4.78[-5]	7.10[-2]	3.42[-3]	5.1[-6]
9	$GK6$		1.09[-4]	6.38[-2]	3.14[-3]	5.5[-7]
10	$H2$	55.44	1.57[-4]	1.27[-5]	2.53[-3]	5.5[-7]
11	$GK7$		9.63[-5]	3.51[-2]	1.47[-3]	1.2[-5]
12	$GK8$	-1.28	1.89[-5]	2.02[-3]	1.49[-4]	

bent shapes of the  $E0$ ,  $F0$ , and  $F1$  curves in Fig. 9(a) are not signs of strong spectroscopic perturbations. All these widths are of the order of  $10^{-10}$ – $10^{-8}$   $\text{cm}^{-1}$ , i.e., rather narrow. This conclusion is in agreement with the corresponding term series dependence displayed in Fig. 2(a).

The three remaining curves in Fig. 9(a) are the ones representing the  $E2$ ,  $F4$ , and  $EF8$  level widths. These curves do not display strong signs of avoided crossings in the sense that sudden jumps in the level widths are basically absent. The  $E2$  and  $F4$  levels are still below the  $EF$  barrier edge. This is reflected by their stronger variations  $\sim 10^{-4}$

– $10^{-8}$   $\text{cm}^{-1}$  in comparison with the  $EF8$  widths  $\sim 5 \times 10^{-5}$ – $5 \times 10^{-6}$   $\text{cm}^{-1}$  for  $J=0$ – $10$ . The  $E2$  width decreases from  $10^{-4}$  to  $10^{-5}$   $\text{cm}^{-1}$  within  $J=0$ – $3$ , from  $10^{-5}$  to  $10^{-8}$   $\text{cm}^{-1}$  within  $J=3$ – $9$ , and increases by about one order of magnitude when going from  $J=9$  to  $10$ . When comparing this behavior with the  $E2$  term series, displayed in Fig. 2(a), the overall impression is that these two graphical representations agree with each other. The rather steep inclination in the beginning of the  $E2$  term series becomes more flat at about  $J=3$ – $4$ . This is due to a repulsion from the  $F4$  term series. Up to that point, the decrease of the corresponding width is

TABLE VIII. The  $\bar{H}$  energy shift differences  $\delta E_{c-o}^{\bar{H}}(v, 0)$  ( $\text{cm}^{-1}$ ) between the present and the levels (observed or computed) reported in Ref. [41], and our calculated widths  $\Gamma_k^{\bar{H}}(v, 0)$  ( $\text{cm}^{-1}$ ) ( $k=4, 5, 5b, 6$ ).

	$s$	$\delta E_{c-o}^{\bar{H}}$	$\Gamma_4^{\bar{H}}$	$\Gamma_5^{\bar{H}}$	$\Gamma_{5b}^{\bar{H}}$	$\Gamma_6^{\bar{H}}$
1	$\bar{H}0$	0	6.96[-7]	7.38[-7]	3.68[-7]	7.44[-7]
2	$\bar{H}1$	2.84	1.77[-6]	1.69[-7]	1.36[-8]	1.08[-6]
3	$\bar{H}2$	3.13	1.45[-5]	1.58[-5]	1.12[-5]	1.60[-5]
4	$\bar{H}3$	6.07	4.74[-5]	4.90[-5]	1.27[-5]	4.95[-5]
5	$\bar{H}4$	8.41	5.38[-5]	6.21[-5]	2.74[-5]	6.16[-5]
6	$\bar{H}5$	10.58	7.51[-5]	8.74[-5]	1.02[-4]	8.80[-5]
7	$\bar{H}6$	21.64	9.47[-5]	1.05[-4]	1.06[-4]	1.02[-4]
8	$\bar{H}7$	24.50	8.85[-5]	1.69[-4]	2.07[-4]	1.61[-4]
9	$\bar{H}8$	27.04	4.00[-5]	7.35[-5]	1.31[-4]	6.93[-5]
10	$\bar{H}9$	29.56	5.47[-6]	3.64[-5]	3.04[-4]	4.01[-5]
11	$\bar{H}10$	31.92	2.49[-4]	2.34[-4]	3.74[-4]	2.44[-4]
12	$\bar{H}11$	33.58	2.86[-4]	6.53[-4]	2.39[-4]	4.50[-4]
13	$\bar{H}12$	34.65	4.46[-3]	4.45[-3]	5.00[-4]	3.93[-3]
14	$\bar{H}13$	32.48	0.29	0.21	0.37	0.23
15	$\bar{H}14$	35.61	0.55	1.26	0.19	1.00
16	$\bar{H}15$	32.50	7.75	11.25	7.12	7.41

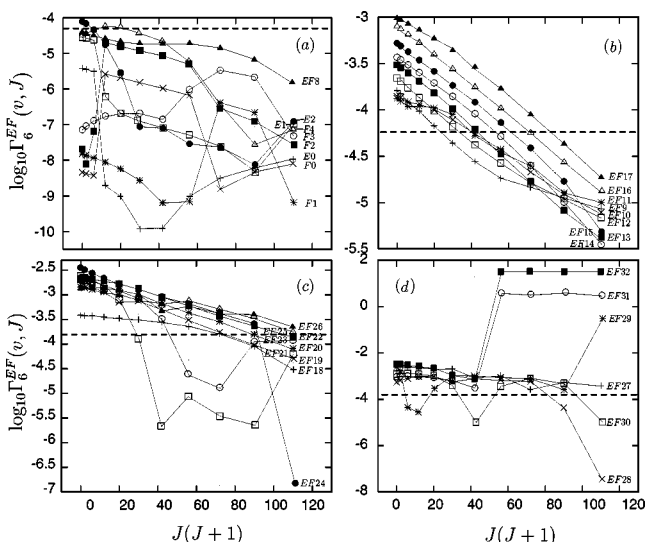


FIG. 9. The  $J(J+1)$  dependence of the logarithm for calculated widths  $\Gamma_6^{EF}(v, J)$  for  $J=0-10$ .

less than one order of magnitude. Within the  $J=3-9$  interval, where the  $E2$  term series is less steep, the gap between each rotational energy and the  $EF$  barrier edge of the corresponding effective potential, displayed in Fig. 2(b), increases. This is reflected by the decrease of the width as functions of  $J(J+1)$ . At  $J=9$  an avoided crossing appears between the  $E2$  and  $F3$  term series. This raises the  $E2$  energy for  $J=10$  a little. At the same time the corresponding width increases by about one order of magnitude. The  $F4$  widths may be analyzed in a similar way.

The  $EF8$  rotational energies for  $J=0-10$  are all positioned above the barrier edge in the corresponding  $EF$  effective potential. This is clearly reflected by the dependence of the corresponding level widths. Within the interval  $J=0-10$  they display a smooth variation, slowly decreasing by about one order of magnitude, starting from  $\Gamma_6^{EF}(v, 0)=4.01 \times 10^{-5} \text{ cm}^{-1}$ . An inspection of the energy gap, between each rotational energy and its effective potential barrier edge, shows that this distance varies little. This is most likely the reason for the smooth nonlinear shape of the  $EF8$  curve in

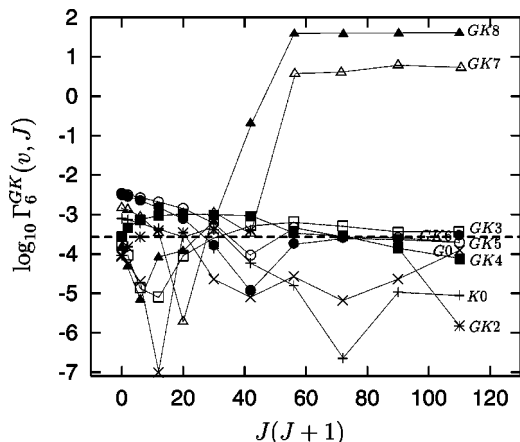


FIG. 10. The  $J(J+1)$  dependence of the logarithm for calculated widths  $\Gamma_6^{GK}(v, J)$  for  $J=0-10$ .

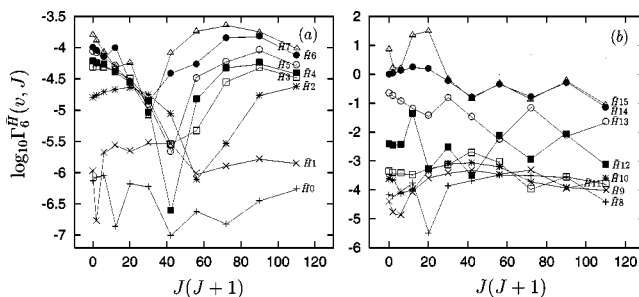


FIG. 11. The  $J(J+1)$  dependence of the logarithm for calculated widths: (a)  $\Gamma_6^H(v=0-7, J)$  and (b)  $\Gamma_6^H(v=8-15, J)$  for  $J=0-10$ .

Fig. 9(a). Although most of the widths in Fig. 9(a) are varying considerably within the  $J=0-10$  interval, we know from the analysis of the rovibronic term series that these variations generally do not originate from homogeneous spectroscopic perturbations from other electronic potential-energy curves. The sudden jumps in the  $EF$  level widths discussed above rather reflect the nonadiabatic effects appearing in the  $EF$  double-well potential.

In Fig. 9(b) we have entered a region where, according to the rovibronic energy analysis, we know that spectroscopic perturbations are very weak or absent. The  $EF9-EF11$  widths are found to be little affected by the double-well structure, while  $EF12-EF17$  display a more linear behavior. All presented  $EF9-EF17$  widths are within  $10^{-6}-10^{-3} \text{ cm}^{-1}$ .

The  $EF18-EF26$  widths are presented in Fig. 9(c). Here we have reached the energy region where both  $GK$  and  $H$  rovibronic levels appear. According to the plot, the  $EF18-EF20$ ,  $EF22$ , and  $EF24-EF26$  widths are only weakly perturbed. Most of these widths are within  $10^{-4}-10^{-2} \text{ cm}^{-1}$ , with the exception of  $\Gamma_6^{EF}(24, 10)=1.3 \times 10^{-7} \text{ cm}^{-1}$ . The  $EF21$  and  $EF23$  widths are strongly varying, indicating that spectroscopic perturbations exist. When comparing these variations with the conclusions from the rovibronic energy analysis, the  $EF21$  levels should be essentially unperturbed, while the  $EF23$  levels are weakly perturbed. The behavior of these widths look similar to the  $F0$  and  $F1$  widths displayed in Fig. 9(a). The  $EF21$  vibrational level is below the  $GK$  barrier and, according to Yu and Dressier [12], it is mainly a mixture of  $EF$  (70%) and  $GK$  (20%) characters. Taking that into account and the fact that at that energy, the  $GK$  potential has a double-well shape similar to that of the  $EF$  potential, one may qualitatively explain the variation of these widths in the same way as was previously done for the  $F0$  and  $F1$  levels. The  $EF23$  rovibronic levels lie above the  $GK$  barrier but the corresponding widths display a similar behavior as the  $EF21$  widths. The  $EF22$  levels, in between these two, are positioned around the  $GK$  barrier but do not seem to be considerably affected with respect to variations. Finally we consider the  $EF27-EF32$  widths displayed in Fig. 9(d). First we note that most of these higher levels have widths within the interval  $10^{-4}-10^{-2} \text{ cm}^{-1}$ . This should be compared with the lowest  $EF$  levels, which all have widths within  $10^{-10}-10^{-4} \text{ cm}^{-1}$ . This verifies that we are here dealing with levels approaching the  $EF$  dissociation limit.

The  $EF27$  widths are all about  $10^{-3} \text{ cm}^{-1}$  within  $J=0-10$ . This, almost constant behavior, agrees with the

shape of the corresponding *EF27* term series. The *EF28* term series do not show any strong signs of spectroscopic perturbations within  $J=0-8$ . This is in agreement with the linear behavior of the corresponding term series discussed above. For  $J=9$  and  $10$  the *EF28* rotational energies are pushed upwards. This is reflected by the jumps observed in the corresponding widths. Why these widths, particularly for  $J=10$ , become smaller is not clear but a partial reason might be due to an interaction with the *GK* state. The *EF29* widths vary more than the *EF27* and *EF28* widths. At  $J=3$  there is a local minimum of about  $5 \times 10^{-5} \text{ cm}^{-1}$ . When  $J$  goes from  $5$  to  $9$ , the width curve displays an almost constant behavior around  $10^{-3} \text{ cm}^{-1}$ . For  $J=10$  a sudden increase of about three orders of magnitude occurs. The dependence of the *EF29* widths agree with the corresponding term values within  $J=0-9$ . The jump at  $J=10$  is more difficult to explain but the existence of the *GK*, and perhaps the *H*, states might be the reason. The *EF30* widths display a similar behavior as the *EF29* widths, but here the local minimum ( $\sim 10^{-5} \text{ cm}^{-1}$ ) appears at  $J=6$ . The decrease from about  $10^{-3}$  to  $10^{-5} \text{ cm}^{-1}$ , for  $J=9-10$ , may partly be explained from the behavior of the corresponding interval for the *EF30* term series. That is, the gap between the rotational energy and the edge of the effective potential for  $J=0-10$  increases. The *EF31* and *EF32* widths are all about  $10^{-3} \text{ cm}^{-1}$  within  $J=0-6$ . Between  $J=7-10$ , all *EF31* and *EF32* widths increase by about five orders of magnitude and thus become very broad. Furthermore, the horizontal dependence of these widths in Fig. 9(d) indicates a bound-state continuum interaction. This is in agreement with the behavior of the corresponding term series, for which it was concluded that the *EF* (and *GK*) threshold had been reached.

### 2. The *GK* and *H* widths

The rotationless level widths,  $\Gamma_k^{GK}(v,0)$  and  $\Gamma_k^H(v,0)$  ( $k=4,5,6$ ), are presented in Table VII. A general conclusion, when inspecting this table, is that  $\Gamma_4^{GK}(v,0) < \Gamma_6^{GK}(v,0) < \Gamma_5^{GK}(v,0)$ , while the *H* widths behave more irregularly. Among these, the most interesting widths to study with respect to the rovibronic dependence are  $\Gamma_6^{GK,H}(v,J)$ , i.e., results based on calculations using the  $(1-6)^1\Sigma_g^+$  manifold.

The rather detailed analysis of the *EF* widths discussed earlier can also be applied on the *GK* widths displayed in Fig. 10. The structure of the *GK* widths is rather dense, particularly for the *GK2-GK6* levels. According to the term series analysis, the *K0* and *G0* rovibronic spectra should be only weakly perturbed. The *K0* and *G0* indeed vary within  $J=0-10$  but it is rather difficult to give a detailed explanation of the irregularities in these widths. However, from Fig. 10, we conclude that  $\Gamma_6^{G0}(v,J) \sim 10^{-7}-10^{-3} \text{ cm}^{-1}$  within  $J=0-10$ . This variation may only partly be understood by studying the corresponding *K0* term series. There should exist, at the moment unknown, additional reasons for these irregularities. The *G0* width has a distinct minimum of about  $10^{-7}$  at  $J=3$  but have values within the range  $10^{-5}-10^{-4} \text{ cm}^{-1}$  for all the other,  $J=0-2$  and  $J=4-10$ , quantum numbers. The *G0* term series does not give any indica-

tion of the sudden jump of  $\Gamma_6^{K0}(v,J)$ , but one suggestion is that it might be a spectroscopic perturbation, due to the *EF* state, which is responsible.

A difference here, from the previous lowest *EF* vibrational levels, is that we have several possible sources of perturbations. Apart from the *GK* double-well potential, we have to consider homogeneous spectroscopic perturbations originating from the *EF* and/or *H* electronic states. The structure of the *GK2-GK6* widths is rather dense which might reflect the homogeneous perturbations predicted for this overlapping energy region. A general observation here is that all widths are within  $10^{-5}-10^{-3} \text{ cm}^{-1}$ . The *GK7-GK8* levels for  $J=0-5$  behave essentially like the *GK2-GK6* levels, but for  $J=6-10$  the corresponding rovibronic levels have reached the threshold. This is clearly seen in Fig. 10, where the *GK7-GK8* widths for  $J=7-10$  are positioned along an almost horizontal line, indicating bound-state continuum level interactions.

### 3. The $\bar{H}$ widths

We also computed widths for the  $\bar{H}0-\bar{H}15$  levels. The rotationless  $\bar{H}$  widths are collected in Table VIII. When comparing the  $\Gamma_4^{\bar{H}}(v,0)$ ,  $\Gamma_5^{\bar{H}}(v,0)$ , and  $\Gamma_6^{\bar{H}}(v,0)$  widths, these are found to be of the same order of magnitude within each vibrational level. For the  $\bar{H}0-\bar{H}12$  levels, the widths vary from  $7 \times 10^{-7}$  to  $4 \times 10^{-3} \text{ cm}^{-1}$ . The  $\bar{H}13-\bar{H}15$  levels are approaching the  $H\bar{H}$  barrier edge. Consequently, their widths become broader and are of the order of a few inverse centimeters.

The fourth set of widths in Table VIII, denoted as  $\Gamma_{5b}^{\bar{H}}$ , were computed from the  $(2-6)^1\Sigma_g^+$  manifold. Most of these widths are of the same order of magnitude as  $\Gamma_4^{\bar{H}}(v,0)$ ,  $\Gamma_5^{\bar{H}}(v,0)$ , and  $\Gamma_6^{\bar{H}}(v,0)$  which reflects the fact that the predissociation of the  $\bar{H}$  levels is mainly not due to the ground state.

The rovibronic width dependence were computed for each of the  $\bar{H}0-\bar{H}15$  levels. The results for the  $(1-6)^1\Sigma_g^+$  manifold are displayed in Fig. 11. Due to the rather dense structure, the data have been divided into two parts. The  $\bar{H}0-\bar{H}1$  widths, displayed in Fig. 11(a), are seen to jump up and down but the variation is rather small, about one order of magnitude for  $J=0-10$ . The  $\bar{H}2-\bar{H}7$  widths, presented in the same figure, behave more smoothly and display a local minimum for  $J=4-6$ . This smooth behavior with the exception of the  $\bar{H}8$ ;  $J=4$  level, continues for the  $\bar{H}8-\bar{H}11$  widths displayed in Fig. 11(b). The variation for these widths is within one order of magnitude. The  $\bar{H}12-\bar{H}15$  widths are rather broad (from  $10^{-3}$  to several inverse centimeters) and do not behave smoothly within  $J=0-10$ . According to the previous study of the  $\bar{H}0-\bar{H}15$  rovibronic energies, these variations are not due to spectroscopic perturbations from other electronic states. One possible reason might be the rather wide and unusual shape of the  $\bar{H}$  potential well (see Fig. 1). In a more detailed analysis of these, and the other

rovibronic  $\bar{H}$  widths discussed here, it would be convenient to plot the corresponding effective potentials for  $J=0-10$ . However, such an analysis is not carried out in the present study.

#### 4. The $H\bar{H}$ widths

For the rotationless levels, not presented here, we found that  $\Gamma_4^{HH}(v,0)$  varies between 8.0 and 67.1  $\text{cm}^{-1}$ ,  $\Gamma_5^{HH}(v,0)$  between 3.5 and 201.3  $\text{cm}^{-1}$ , and  $\Gamma_6^{HH}(v,0)$  between 9.8 and 110.3  $\text{cm}^{-1}$ , with the exception that  $\Gamma_5^{HH}(1,0)=0.41 \text{ cm}^{-1}$ . Thus, here we are dealing with strongly predissociated levels.

For the rovibronic levels ( $v,0-10$ ), the  $\log_{10} \Gamma_k^{HH}(v,J)$  ( $k=4,5,6$ ) dependence on  $J(J+1)$  did not indicate any strong perturbations. The rovibronic widths are all of the same order of magnitude as the rotationless ones although they vary within each ( $v,J$ ) sequence for  $J=0-10$ . Due to the large size (from a few to  $\sim 100 \text{ cm}^{-1}$ ) of these widths, a graphical representation is not meaningful from a physical point of view. Just as we suggested for the  $\bar{H}$  widths, a reason for the size and variation of the  $H\bar{H}$  widths is most likely the wide shape of the  $H\bar{H}$  potential well. This shape is more sensitive to changes than a deep and narrow well when calculating effective potentials. Thus, the wave functions, associated with the corresponding rovibronic levels, become less localized than they would be for a deeper and more narrow potential well.

#### 5. The $HPO$ widths

The  $HPO$  level width dependence was also studied but, in order to limit the amount of presented data, we just present a short summary here. A further reason is that most of these levels are strongly predissociated. In general, the  $H0-H2$  widths vary between  $10^{-4}-10^{-1} \text{ cm}^{-1}$  except that  $\Gamma_6^H(1,10)=0.18 \times 10^{-6} \text{ cm}^{-1}$ . The perturbations discussed earlier may be the reason for these variations. A few of the lowest rotational energies of the lowest  $P$  vibrational level have widths of the order of  $10^{-2} \text{ cm}^{-1}$ , while the other  $HPO$  widths are of the order of  $10^{-1}-10^2 \text{ cm}^{-1}$ . However, according to the uncertainty in the identification of the  $HPO$  energy spectra, we should be careful with drawing conclusions about a specific level.

#### C. Nonradiative lifetimes

From the relation, the nonradiative lifetime was obtained for each computed level. Our rotationless results  $\tau_k^s(v,0)_{nr}$  are listed in Tables IX–XI.

According to Table IX, the rotationless  $EF$  nonradiative lifetimes vary within the intervals  $\tau_4^{EF}(v,0)_{nr}=22.99 \text{ ns}-59.33 \text{ ms}$ ,  $\tau_5^{EF}(v,0)_{nr}=73.95 \text{ ns}-1.17 \text{ ms}$ , and  $\tau_6^{EF}(v,0)_{nr}=1.49 \text{ ns}-1.15 \text{ ms}$ . For lower vibrational levels the mutual magnitude of these lifetimes seems to vary randomly, while for  $EF10-EF32$  they generally vary as  $\tau_6^{EF}(v,0)_{nr} < \tau_4^{EF}(v,0)_{nr} < \tau_5^{EF}(v,0)_{nr}$ .

TABLE IX. The present calculated  $EF$  nonradiative lifetimes  $\tau_k^{EF}(v,0)$  (ms,  $\mu\text{s}$ , ns) ( $k=4,5,6$ ), and the theoretical results  $\tau_a^{EF}(v,0)$  (ms,  $\mu\text{s}$ , ns) from Ref. [11].

	$s$	$\tau_4^{EF}$	$\tau_5^{EF}$	$\tau_6^{EF}$	$\tau_a^{EF}$
1	$E0$	17.82 $\mu\text{s}$	251.66 $\mu\text{s}$	1.40 $\mu\text{s}$	354 ms
2	$F0$	59.33 ms	1.17 ms	1.15 ms	61.7 ms
3	$F1$	15.80 ms	319.88 $\mu\text{s}$	351.61 $\mu\text{s}$	5.8 ms
4	$E1$	37.13 $\mu\text{s}$	24.03 $\mu\text{s}$	186.32 ns	27.6 $\mu\text{s}$
5	$F2$	116.70 $\mu\text{s}$	38.76 $\mu\text{s}$	256.52 $\mu\text{s}$	5.8 ms
6	$F3$	18.70 $\mu\text{s}$	11.52 $\mu\text{s}$	73.75 ns	15.6 ms
7	$E2$	593.30 ns	11.37 $\mu\text{s}$	67.05 ns	252.9 $\mu\text{s}$
8	$F4$	5.80 $\mu\text{s}$	2.52 $\mu\text{s}$	165.42 ns	885.0 $\mu\text{s}$
9	$EF8$	4.18 $\mu\text{s}$	1.64 $\mu\text{s}$	132.42 ns	252.9 $\mu\text{s}$
10	$EF9$	402.27 ns	1.49 $\mu\text{s}$	990.67 ns	31.2 $\mu\text{s}$
11	$EF10$	338.22 ns	4.43 $\mu\text{s}$	37.93 ns	29.5 $\mu\text{s}$
12	$EF11$	408.46 ns	333.96 $\mu\text{s}$	39.93 ns	44.3 $\mu\text{s}$
13	$EF12$	366.21 ns	275.13 $\mu\text{s}$	24.03 ns	183.1 $\mu\text{s}$
14	$EF13$	351.66 ns	800.90 $\mu\text{s}$	17.35 ns	156.2 $\mu\text{s}$
15	$EF14$	293.37 ns	86.06 $\mu\text{s}$	14.31 ns	16.6 $\mu\text{s}$
16	$EF15$	158.04 ns	4.08 $\mu\text{s}$	10.11 ns	7.8 $\mu\text{s}$
17	$EF16$	74.06 ns	951.61 ns	6.65 ns	7.7 $\mu\text{s}$
18	$EF17$	44.62 ns	438.84 ns	5.42 ns	35.4 $\mu\text{s}$
19	$EF18$	62.03 ns	735.46 ns	13.83 ns	8.3 $\mu\text{s}$
20	$EF19$	27.23 ns	180.61 ns	3.22 ns	27.9 ms
21	$EF20$	27.37 ns	95.85 ns	3.66 ns	7.1 $\mu\text{s}$
22	$EF21$	45.38 ns	73.95 ns	2.19 ns	35.4 $\mu\text{s}$
23	$EF22$	22.99 ns	399.25 ns	2.50 ns	221.3 $\mu\text{s}$
24	$EF23$	30.00 ns	122.92 ns	2.40 ns	983.3 ns
25	$EF24$	22.99 ns	119.33 ns	1.49 ns	5.8 $\mu\text{s}$
26	$EF25$	28.55 ns	536.91 ns	2.75 ns	531.0 ns
27	$EF26$	29.50 ns	8.09 $\mu\text{s}$	3.96 ns	672.2 ns
28	$EF27$	29.66 ns	3.43 $\mu\text{s}$	2.10 ns	1.3 $\mu\text{s}$
29	$EF28$	58.35 ns	172.96 ns	9.74 ns	3.3 $\mu\text{s}$
30	$EF29$	164.40 ns	418.11 ns	2.10 ns	3.1 $\mu\text{s}$
31	$EF30$	71.56 ns	3.77 $\mu\text{s}$	4.25 ns	5.6 $\mu\text{s}$
32	$EF31$	30.34 ns	408.46 $\mu\text{s}$	1.59 ns	71.8 $\mu\text{s}$
33	$EF32$	125.83 ns	3.71 $\mu\text{s}$	5.58 ns	1.5 $\mu\text{s}$

The rotationless  $GK$  and  $H$  nonradiative lifetimes are presented in Table X. The  $GK$  results vary within the intervals  $\tau_4^{GK}(v,0)_{nr}=55.14 \text{ ns}-10.21 \text{ ms}$ ,  $\tau_5^{GK}(v,0)_{nr}=83.23 \text{ ps}-3.18 \text{ ns}$ , and  $\tau_6^{GK}(v,0)_{nr}=1.55 \text{ ns}-62.03 \text{ ns}$ . The corresponding  $H$  results are  $\tau_4^H(v,0)_{nr}=33.82 \text{ ns}-47.41 \mu\text{s}$ ,  $\tau_5^H(v,0)_{nr}=44.25 \text{ ns}-3.36 \mu\text{s}$ , and  $\tau_6^H(v,0)_{nr}=2.10 \text{ ns}-593.96 \text{ ns}$ . For the mutual magnitude of  $GK$  as well as  $H$ , lifetimes vary from level to level.

The rotationless  $\bar{H}$  nonradiative lifetimes are presented in Table XI. Here, the  $\tau_4^{\bar{H}}(v,0)_{nr}$ ,  $\tau_5^{\bar{H}}(v,0)_{nr}$ , and  $\tau_6^{\bar{H}}(v,0)_{nr}$  results are found to be about the same magnitude within each vibrational level. For the  $\bar{H}0-\bar{H}12$  levels, these lifetimes are within 1.19 ns–31.42  $\mu\text{s}$ . The  $\bar{H}13-\bar{H}15$  levels approach the local  $H\bar{H}$  barrier edge and, consequently, their lifetimes be-

TABLE X. The present calculated  $GK$  and  $H$  nonradiative lifetimes  $\tau_k^{GK,H}(v,0)$  ( $\mu\text{s}$ , ns, ps) ( $k=4,5,6$ ), and the theoretical results  $\tau_a^{EF}(v,0)$  ( $\mu\text{s}$ , ns) from Ref. [11].

	$s$	$\tau_4^s$	$\tau_5^s$	$\tau_6^s$	$\tau_a^s$
1	$K0$	127.95 ns	358.8 ps	6.69 ns	2.9 $\mu\text{s}$
2	$G0$	656.37 ns	2.20 ns	62.03 ns	3.3 $\mu\text{s}$
3	$H0$	7.68 $\mu\text{s}$	44.25 ns	593.96 ns	15.2 $\mu\text{s}$
4	$GK2$	60.07 ns	1.78 ns	57.47 ns	2.0 $\mu\text{s}$
5	$GK3$	2.70 $\mu\text{s}$	3.18 ns	32.18 ns	1.0 $\mu\text{s}$
6	$GK4$	10.21 $\mu\text{s}$	1.02 ns	19.31 ns	295.0 ns
7	$H1$	47.41 $\mu\text{s}$	3.35 $\mu\text{s}$	21.50 ns	3.3 $\mu\text{s}$
8	$GK5$	111.09 ns	74.79 ps	1.55 ns	1.0 $\mu\text{s}$
9	$GK6$	48.72 ns	83.23 ps	1.69 ns	9.7 $\mu\text{s}$
10	$H2$	33.82 ns	418.11 ns	2.10 ns	9.7 $\mu\text{s}$
11	$GK7$	55.14 ns	151.28 ps	3.61 ns	442.5 ns
12	$GK8$	280.95 ns	2.63 ns	35.64 ns	

come shorter, typically of the order of ps. From the discussion on the  $\bar{H}$  widths we know that the predissociation is mainly not due to the ground state. This is reflected here by the  $\tau_{5b}^H(v,0)_{nr}$  lifetimes computed for the  $(2-5)^1\Sigma_g^+$  manifold. Although these lifetimes differ somewhat from the  $\tau_{4-6}^H(v,0)_{nr}$  results, these are all of the same order of magnitude.

Instead of giving a detailed analysis of the rovibronic nonradiative lifetimes we refer to the discussions on the corresponding widths, as these two quantities are directly re-

TABLE XI. The present calculated  $\bar{H}$  nonradiative lifetimes  $\tau_k^{GK,H}(v,0)$  ( $\mu\text{s}$ , ns, ps) ( $k=4,5,5b,6$ ).

	$s$	$\tau_4^{\bar{H}}$	$\tau_5^{\bar{H}}$	$\tau_{5b}^{\bar{H}}$	$\tau_6^{\bar{H}}$
1	$\bar{H}0$	7.63 $\mu\text{s}$	7.20 $\mu\text{s}$	14.43 $\mu\text{s}$	7.14 $\mu\text{s}$
2	$\bar{H}1$	3.00 $\mu\text{s}$	31.42 $\mu\text{s}$	390.44 $\mu\text{s}$	4.92 $\mu\text{s}$
3	$\bar{H}2$	366.21 ns	336.08 ns	474.11 ns	331.88 $\mu\text{s}$
4	$\bar{H}3$	112.03 ns	108.37 ns	418.11 $\mu\text{s}$	107.27 $\mu\text{s}$
5	$\bar{H}4$	98.70 ns	85.51 ns	193.80 ns	86.20 $\mu\text{s}$
6	$\bar{H}5$	70.71 ns	60.76 ns	52.06 ns	60.34 $\mu\text{s}$
7	$\bar{H}6$	56.07 ns	50.57 ns	50.09 ns	52.06 $\mu\text{s}$
8	$\bar{H}7$	60.00 ns	31.42 ns	25.65 ns	32.98 $\mu\text{s}$
9	$\bar{H}8$	132.75 ns	74.24 ns	40.53 ns	76.62 $\mu\text{s}$
10	$\bar{H}9$	970.75 ns	145.88 ns	17.47 ns	132.42 $\mu\text{s}$
11	$\bar{H}10$	21.33 ns	22.69 ns	14.20 ns	21.76 $\mu\text{s}$
12	$\bar{H}11$	18.57 ns	8.13 ns	22.22 ns	11.80 $\mu\text{s}$
13	$\bar{H}12$	1.19 ns	1.19 ns	10.62 ns	1.35 $\mu\text{s}$
14	$\bar{H}13$	18.31 ps	25.29 ps	14.35 ps	23.09 ps
15	$\bar{H}14$	9.65 ps	4.21 ps	27.95 ps	5.31 ps
16	$\bar{H}15$	0.69 ps	0.47 ps	0.75 ps	0.72 ps

lated. From this relation it is easy to imagine the graphical structure of the rovibronic lifetimes by studying the widths displayed in Figs. 9–11.

#### D. Estimations of spectroscopically measurable rovibronic levels

Many of the level widths reported in the present paper are rather narrow. This implies that the corresponding levels have nonradiative lifetimes long enough to be spectroscopically measurable. In order to obtain estimations of such levels we first have to assume that their radiative lifetimes,  $\tau_r(v,J)$ , vary smoothly with  $J$  within a rovibronic term series [43,44]. From this we can estimate a lower limit,  $\tau_r^{\min}(v,J)$ , for which a level might be experimentally observable. The second assumption is that we consider levels for which  $\tau_r(v,J) \approx \tau_{nr}(v,J)$ , where  $\tau_{nr}(v,J)$  are our calculated nonradiative lifetimes. Thus, from experimentally obtained radiative lifetimes, we are able to suggest spectroscopically measurable rovibronic levels which have not yet been experimentally observed.

According to Kiyoshima and Sato [45], the observed lifetimes of the rovibronic  $EF6$  and  $EF7$  levels vary smoothly within the interval  $J=0-4$ . The  $EF6$  lifetimes  $\tau_r^{EF}(6,J)$  increase from  $101 \pm 2$  ns to  $170 \pm 9$  ns when  $J$  goes from 0 to 4, while  $\tau_r^{EF}(7,J)$  decrease from  $246 \pm 13$  ns to  $129 \pm 6$  ns within the same interval. Assuming this behavior to be true also for other  $EF$  levels we may use the calculations of Glass-Maujean *et al.* [46] to estimate a lower limit for the radiative lifetimes. By analyzing the available experimental [45,47] and theoretical [46] data we found that for  $EF$  levels below the  $GK$  spectra, the shortest measured radiative lifetime is  $\tau_r=100.0$  ns for the  $EF6$  level. This is further supported by the calculations carried out by Glass-Maujean *et al.* [46]. They obtained a nonadiabatic,  $\tau_r=99.0$  ns ( $J=0$  and 1), as well as an adiabatic,  $\tau_r=100.0$  ns ( $J=1$ ), result for the  $EF6$  level. Their other computed  $EF$  lifetimes in the same energy region are in all cases longer, typically several hundreds of nanoseconds. From these, theoretical and experimental results, a lower limit for the radiative lifetimes was chosen to be 100.0 ns which corresponds to  $\log_{10} \Gamma_{max} = -4.27$ . This maximum value is indicated by the dashed line in Figs. 9(a) and 9(b) and should be interpreted in such a way that  $EF$  levels having logarithmic widths smaller than  $\log_{10} \Gamma_{max}$  may be spectroscopically measurable.

For higher  $EF$  levels, an experimental rotationless lifetime of  $\tau_r=48.5$  ns [48] was found for the  $EF26$  level. All calculated adiabatic and nonadiabatic radiative  $EF$  lifetimes for  $J=0$ , presented by Glass-Maujean *et al.* [46], are considerably longer, while their nonadiabatic  $EF26$  result for  $J=1$  was calculated to be  $\tau_r=34.5$  ns. This corresponds to a limit  $\log_{10} \Gamma_{max} = -3.81$ , which is indicated by the dashed line in Figs. 9(c) and 9(d).

For the  $GK$  spectra we found the shortest experimental lifetime  $\tau_r=24.8$  ns [49] for the  $G0$  level (denoted as  $GK1$  in Ref. [46]). The corresponding nonadiabatic,  $J=0$  and 1, result is  $\tau_r=20.8$  ns, while the calculated adiabatic value for  $J=1$  is 18.1 ns. Choosing the nonadiabatic results as the limit, we find that  $\log_{10} \Gamma_{max} = -3.59$ , which is indicated in

Fig. 10. Here, approximately half of the levels are seen to have their logarithmic widths below this limit. It is also clear from the figure that all nine  $GK$  vibrational levels have at least some rotational level within  $J=0-10$  which may be spectroscopically measurable.

Finally, we consider the  $H0-H2$  levels. For these three characters we do not have any experimental results for the radiative lifetimes. Therefore, we again use the adiabatic and nonadiabatic results reported by Glass-Maujean [46]. The shortest adiabatic radiative lifetime,  $\tau_r=27.6$  ns, is found for the  $H2(J=1)$  level, while the corresponding nonadiabatic result is  $\tau_r=28.6$  ns. From the latter result we find a limit of  $\Gamma_{max}=1.86\times 10^{-4}\text{cm}^{-1}$  in the sense that all widths less than this limit may be spectroscopically measurable. We do not present our calculated rovibronic widths for  $H0-H2$  graphically but a comparison, between our  $(1-6)^1\Sigma_g^+$  results with  $\Gamma_{max}$  given above, can be summarized as  $\Gamma_6^{H0}(v,J)<\Gamma_{max}$  for  $J=0-4$  and  $6-10$ ,  $\tau_6^{H1}(v,J)<\Gamma_{max}$  for  $J=9$  and  $10$ , and  $\Gamma_6^{H2}(v,J)<\Gamma_{max}$  for  $J=9$  and  $10$ .

The above analysis as well as our choice of limits for the  $EF$ ,  $GK$ , and  $H$  levels, is rather simplified. For the  $EF$  spectra the comparable data for lower levels is rather good but for higher  $EF$  levels as well as for the  $GK$  and  $H$  spectra, it is rather poor. With a larger amount of experimental data, particularly for higher rotational levels, one would most likely find more appropriate limits for each of these terms.

## E. Comparisons with experiments and other calculations

### 1. The energy levels

In order to compare our computed rotationless energies with observed term values we used the manifold consisting of the first five excited states,  $(2-6)^1\Sigma_g^+$ , as they all originate from the same source [4]. However, for reasons already discussed earlier, we compared the differences between adjacent levels calculated here with the corresponding differences of known observed term values [12,41]. These comparisons are collected in Tables VI–VIII. Using the notation  $\delta E_{c-o}^s(v,0)=\Delta E_{calc}^s(v,0)-\Delta E_{obs}^s(v,0)$ , where the indices *calc* and *obs* refer to our computed energies and observed term values, respectively, we found that  $|\delta E_{c-o}^{EF}(v,0)|$  varies between 0.01 and 9.18  $\text{cm}^{-1}$ , but for most of the levels this discrepancy is  $\sim 0-2$   $\text{cm}^{-1}$ . Note that the labels  $EF8$  and  $EF9$  in Table VI correspond to  $F5$  and  $E3$  in Ref. [12].

For the  $GK$  levels,  $\delta E_{c-o}^{GK}(v,0)$  varies between  $-4.43$  ( $GK5$ ) and  $18.67$   $\text{cm}^{-1}$  ( $G0$ ). Qualitatively, these discrepancies agree with the  $EF$  results in the sense that the  $EF$  levels within the same energy region suddenly demonstrate larger  $\delta E_{c-o}^{EF}$  shifts. Also the  $H0-H2$  are within the same range, which is reflected by the discrepancies  $\delta E_{c-o}^{H1}(v,0)=21.48$   $\text{cm}^{-1}$  and  $\delta E_{c-o}^{H2}(v,0)=55.44$   $\text{cm}^{-1}$ .

Our theoretical  $\bar{H}$  energy shifts were compared with the experimentally observed and calculated  $\bar{H}$  energies by Reinhold *et al.* [41]. According to Table VIII, the discrepancies  $\delta E_{c-o}^{\bar{H}}(v,0)$  increase from 2.84  $\text{cm}^{-1}$  to 35.61  $\text{cm}^{-1}$  when going from  $v=0$  to 15.

The discrepancies of  $\delta E_{c-o}^s(v,0)$  discussed above may originate from several different sources. In our previous dis-

ussion we concluded that the overlapping  $EF$ ,  $GK$ , and  $H$  levels were perturbing each other, while for the  $\bar{H}$  levels no such signs were seen. A possible reason for the large discrepancies may be the incomplete set of electronic singlet states used in our calculations. Even though we include the ground state when comparing different approximations we exclude it here. The fact that we are here considering only  $^1\Sigma_g^+$  states means that perturbations seen in our spectra are all homogeneous ( $\Delta\Lambda=0$ ). Other states, which appear in the energy region studied here but were excluded in our calculations, are of  $^1\Pi_g$ ,  $^1\Delta_g$  and  $^1\Lambda_g$  character. The possible heterogenous ( $\Delta\Lambda=\pm 1$ ) perturbations originating from these terms are therefore not taken into account. This is most likely one of the reasons why the discrepancies increase higher up in the vibrational level structure.

Another reason might be that relativistic corrections were not included in our calculations. However, according to Ref. [4], these are all of the order of  $-2$   $\text{cm}^{-1}$  at the outer and inner minima of the  $EF$  and  $GK$  potential curves and smaller elsewhere. Therefore, these should not produce any of the shifts discussed above.

### 2. The level widths

To the best of our knowledge, the only directly comparable results here are the rotationless level widths reported in the theoretical predissociation study of  $EF$ ,  $GK$ , and  $H$  states in  $\text{H}_2$  by Quadrelli *et al.* [2]. According to their calculated widths  $\Gamma_a^s(v,0)$  ( $s=EF,GK,H$ ), collected in Tables VI and VII, they found the predissociation to be rather weak for most of these levels. Our corresponding theoretical results,  $\Gamma_k^s(v,0)$ , for the 4-, 5-, and 6-state approximations, presented in the same tables, indicate a somewhat stronger predissociation for most of the levels.

A relevant comparison between our and their computational methods should be based on calculations using the same basis set. Therefore, we now only consider our computed  $\Gamma_4^{EF}(v,0)$ ,  $\Gamma_4^{GK}(v,0)$ , and  $\Gamma_4^H(v,0)$  widths. Beginning with the  $EF$  widths, presented in Table VI, we find that our calculated  $F0$ ,  $F2$ , and  $E1$  widths are of the same order of magnitude as  $\Gamma_a^{EF}(v,0)$  for the corresponding levels. For all other levels,  $\Gamma_4^{EF}(v,0)>\Gamma_a^{EF}(v,0)$  and the difference is, in general, 1–2 orders of magnitude. A similar comparison for the  $GK$  widths presented in Table VII shows a better agreement, but our calculated widths are still generally larger than the results of Quadrelli *et al.* [2]. When comparing the  $H0-H2$  widths in Table VII we find a rather good agreement for the  $H0$  results. Our  $H1$  width is narrower by two orders of magnitude, while our  $H2$  width is wider by three orders of magnitude when compared with the results of Quadrelli *et al.* [2].

Although the differences are generally rather large, between our separate level widths and the corresponding calculated widths of Quadrelli *et al.* [2], it may be interesting to compare relative widths,  $\Gamma(v,0)/\Gamma(v+1,0)$ , between  $\Gamma_4^s(v,0)$  and  $\Gamma_a^s(v,0)$  ( $s=EF,GK,H$ ) presented in Tables VI and VII. If we define a quantity  $\delta\Gamma_4^s(v,0)$  for these comparisons

$$\delta\Gamma_4^s(v,0) = \left| \frac{\Gamma_4^s(v,0)/\Gamma_4^s(v+1,0)}{\Gamma_a^s(v,0)/\Gamma_a^s(v+1,0)} \right|, \quad (40)$$

we find that for a majority of the  $EF$  ( $\sim 75\%$ ) and the  $GK, H$  ( $\sim 70\%$ ) level widths,  $\delta\Gamma_4^{EF}(v,0) \sim 0-1$  orders of magnitude, while for the remaining level widths,  $\delta\Gamma_4^{GK,H}(v,0) \sim 2-5$  orders of magnitude. Thus, the agreement here is somewhat better than what was found for the mutual comparison between the levels themselves.

A similar treatment can, of course, be carried out for the nonradiative lifetimes. The  $\Gamma_a^s(v, J)$  ( $s=EF, GK, H$ ) widths were therefore converted to nonradiative lifetimes  $\tau_a^s(v, J)$  which are presented in Tables IX and X.

A natural reflection here is that the weak predissociation for excited  $EF$ ,  $GK$ , and  $H$  levels in  $H_2$ , generated by coupling to the ground state, reported by Quadrelli *et al.* [2] may be somewhat stronger. A possible reason for the differences between their computed widths and the present results, which are already mentioned in the introductory section, might be the different methods used by us and Quadrelli *et al.* [2]. While their method is based on a golden rule approach, for which the width is calculated from a real valued energy and wave function, our computed widths are included as the imaginary part of converged complex eigenvalues.

## SUMMARY AND CONCLUSIONS

By applying a general Runge-Kutta-Fehlberg method and available nonadiabatic coupling elements, the adiabatic (1-4), (1-5), and (1-6)  $^1\Sigma_g^+$  manifolds of  $H_2$  were transformed to diabatic representations. In order to obtain rovibronic term energy values and level widths, the multichannel Schrödinger equation was solved for each diabatic representation by means of an exterior complex rotated finite element method. The structures of our term values and widths were compared between the three different manifolds. In general, our results verified the homogeneous spectroscopic perturbations reported in the theoretical study by Yu and Dressler [12]. In our analysis we focused on the (1-6)  $^1\Sigma_g^+$  manifold for which most of the rovibronic levels ( $v, J=0-10$ ) were identified. From graphical representations of the various rovibronic energy and width sequences within  $J=0-10$ , we investigated the existence of homogeneous spectroscopic perturbations.

The (1-4)  $^1\Sigma_g^+$  widths, in particular, were compared with the theoretical predissociation study of Quadrelli *et al.* [2]. It was found that our calculated level widths are generally about two orders of magnitude wider than theirs, indicating a somewhat stronger predissociation than previously reported.

From observed and theoretically obtained radiative lifetimes we were able to estimate upper width limits for which our computed rovibronic  $EF$ ,  $GK$ , and  $H$  levels may be experimentally observed.

Concludingly, the present work as well as a number of previous nonadiabatic multichannel studies [13-16] are all based on the same theoretical and numerical approach. By summarizing these results we are here able to draw some general conclusions about our method for predissociation studies of diatomic molecules.

One interesting feature, particularly investigated in the present paper, is how the complex eigenvalues are affected by the number of states included in a diatomic manifold. When, for example, comparing results for the lower rotationless  $EF$  levels in the (1-4), (1-5), and (1-6)  $^1\Sigma_g^+$  manifolds of  $H_2$ , the term values are clearly converged, while the corresponding level widths are seen to vary according to  $\Gamma_5^{EF}(v,0) < \Gamma_4^{EF}(v,0) < \Gamma_6^{EF}(v,0)$ . Some of these widths vary as much as four orders of magnitude when different approximations are compared. This information may be extremely useful as it offers a possibility to understand how a specific rovibronic level is affected when adding one or several more electronic states to the already existing manifold of states.

A more general conclusion, shared by several of the studies considered here, is that diabatic, or approximately diabatic, multichannel calculations generate term values which are usually in a better agreement with experiments than results based on pure Born-Oppenheimer potential-energy curves.

The rovibronic spectra often gives a lot more information than the corresponding rotationless levels. The rotational term series are very useful when identifying the characters of different electronic states included in a manifold. In the case of unperturbed, or only weakly perturbed levels, a term series generally display a linear dependence as a function of  $J(J+1)$ . The inclination of this linear function reflects the shape of the corresponding electronic potential well and thus the character of a specific term series. Simply speaking, the steeper the inclination the narrower the potential well. In the case when significant spectroscopic perturbations exist, the linear term series dependence is often seen to be broken. This is in general a useful information which motivates a further investigation of these levels.

Furthermore, the present as well as the four previous studies [13-16] considered here all demonstrate the importance to include nonradiative widths for many rotational levels as they often vary with several orders of magnitude within a term series. A sudden jump in a width thus indicate if the perturbation seen in the term series plot implies a stronger or weaker predissociation for a specific rovibronic level. From the nonradiative level widths, particularly when these suddenly become narrow, it is convenient to convert to nonradiative lifetimes. By comparing observed and theoretically obtained radiative lifetimes with our nonradiative lifetimes we have, in several of these studies, been able to estimate upper time and width ( $\tau=1/\Gamma$ ) limits for which the corresponding levels may be spectroscopically measurable.

In order to further motivate the usefulness of our complex rotated finite element method for computing the widths we particularly refer to the studies of  $CO^{2+}$  [13] and  $Al_2$  [16]. For  $CO^{2+}$  it was found that our method produced results in a better agreement with experiments when compared with results based on a golden rule approach. In the case of  $Al_2$ , nonradiative lifetimes computed with our method were compared with two other sets of results obtained by different golden rule type methods [5]. Our obtained nonradiative lifetimes were found to be considerably different when compared with the other two sets of nonradiative lifetimes. However, the agreement between the two golden rule type results was found to be rather poor. This disagreement indicates an uncertainty when using the golden rule approach for predissociation studies of diatomic molecules.

sociation studies, particularly when computing level widths (and lifetimes). This weakness, together with the previously discussed proven convergence of our complex eigenvalues, supports the strength and reliability of our method.

Finally, we believe that the present as well as the previous similar predissociation studies [13–16] show the usefulness of our general method for predissociation studies. With our complex rotated finite element code we are able to solve the multichannel Schrödinger equation for any number of coupled electronic states within a diatomic manifold. By

studying and comparing rovibronic term energy values and the corresponding widths, we have achieved some general knowledge about interpretations of the different types of perturbed energy-level structures in diatomic molecules.

#### ACKNOWLEDGMENTS

This work was supported by a grant from the Swedish National Science Foundation (NFR) and by Stockholm University.

- 
- [1] J. von Neumann and E. Wigner, *Phys. Z.* **30**, 467 (1929).  
 [2] P. Quadrelli, K. Dressler, and L. Wolniewicz, *J. Chem. Phys.* **93**, 4958 (1990).  
 [3] L. Wolniewicz and K. Dressler, *J. Chem. Phys.* **82**, 3292 (1985).  
 [4] L. Wolniewicz and K. Dressler, *J. Chem. Phys.* **100**, 444 (1994).  
 [5] S. Han and D. R. Yarkony, *Mol. Phys.* **88**, 53 (1996).  
 [6] X. He, O. Atabek, and A. Giusti-Suzor, *Phys. Rev. A* **42**, 1585 (1990).  
 [7] C. A. Mead and D. G. Truhlar, *J. Chem. Phys.* **77**, 6090 (1982).  
 [8] G. H. Dieke, *Phys. Rev.* **50**, 797 (1936).  
 [9] G. H. Dieke, *Phys. Rev.* **76**, 50 (1949).  
 [10] G. H. Dieke, *J. Mol. Spectrosc.* **2**, 494 (1958).  
 [11] P. Quadrelli, K. Dressler, and L. Wolniewicz, *J. Chem. Phys.* **92**, 7461 (1990).  
 [12] S. Yu and K. Dressler, *J. Chem. Phys.* **101**, 7692 (1994).  
 [13] L. H. Anderssen *et al.*, *Phys. Rev. Lett.* **71**, 1812 (1993).  
 [14] C. Carlsund-Levin, N. Elander, A. Nunez, and A. Scrinzi, *Phys. Scr.* **65**, 306 (2002).  
 [15] S. Andersson and N. Elander, *J. Mol. Spectrosc.* **214**, 103 (2002).  
 [16] S. Andersson and N. Elander, *J. Mol. Spectrosc.* **216**, 15 (2002).  
 [17] J. Aguilar and J. M. Combes, *Commun. Math. Phys.* **22**, 269 (1971).  
 [18] E. Balslev and J. M. Combes, *Commun. Math. Phys.* **22**, 280 (1971).  
 [19] B. Simon, *Ann. Math.* **97**, 247 (1973).  
 [20] C. van Winter, *J. Math. Anal. Appl.* **47**, 368 (1974).  
 [21] C. van Winter, *J. Math. Anal. Appl.* **18**, 633 (1974).  
 [22] L. Wolniewicz, *J. Chem. Phys.* **103**, 1792 (1995).  
 [23] G. Herzberg, *Molecular Spectra and Molecular Structure. Volume I—Spectra of Diatomic Molecules* (Van Nostrand Reinhold, New York, 1950).  
 [24] L. Wolniewicz, *J. Chem. Phys.* **99**, 1851 (1993).  
 [25] R. G. Gordon, *J. Chem. Phys.* **51**, 14 (1969).  
 [26] R. de Vogelaere, *J. Res. Natl. Bur. Stand.* **54**, 119 (1954).  
 [27] P. Quadrelli, K. Dressler, and L. Wolniewicz, *J. Chem. Phys.* **92**, 7461 (1990).  
 [28] M. Baer, *Chem. Phys. Lett.* **35**, 112 (1975).  
 [29] K. Dressler, R. Gallusser, P. Quadrelli, and L. Wolniewicz, *J. Mol. Spectrosc.* **75**, 205 (1979).  
 [30] C. A. Nicolaides and D. R. Beck, *Phys. Lett.* **65A**, 11 (1978).  
 [31] B. Gyarmati and T. Vertse, *Nucl. Phys. A* **160**, 523 (1971).  
 [32] B. Simon, *Phys. Lett.* **71A**, 211 (1979).  
 [33] B. Helffer, in *Resonances*, edited by E. Brändas and N. Elander, Lecture Notes in Physics Vol. 325 (Springer, Berlin, 1989), p. 11.  
 [34] E. Fehlberg, NASA Technical Report No. R-315 (unpublished).  
 [35] L. F. Shampine, H. A. Watts, and S. Davenport, Sandia Laboratories Report No. SAND75-0182 (unpublished).  
 [36] L. Baker, *C Tools for Scientists and Engineers* (McGraw-Hill, Hamburg, 1989).  
 [37] A. Scrinzi and N. Elander, *J. Chem. Phys.* **98**, 3866 (1993).  
 [38] N. Moiseyev, P. R. Certain, and F. Weinhold, *Mol. Phys.* **336**, 1613 (1978); **47**, 585 (1982).  
 [39] A. K. Cline, *Commun. ACM* **17**, 218 (1974).  
 [40] B. H. Bransden and C. J. Joachain, *Physics of Atoms and Molecules* (Longmans, New York, 1983).  
 [41] E. Reinhold, W. Hogerworst, W. Ubachs, and L. Wolniewicz, *Phys. Rev. A* **60**, 1258 (1999).  
 [42] P. Senn and K. Dressler, *J. Chem. Phys.* **87**, 1205 (1987).  
 [43] H. Lefebvre-Brion and R. W. Field, *Perturbations in the Spectra of Diatomic Molecules* (Academic Press, Orlando, 1986).  
 [44] N. Elander, J. Oddershede, and N. H. Beebe, *Astrophys. J.* **216**, 165 (1977).  
 [45] T. Kiyoshima and S. Sato, *Chem. Phys. Lett.* **342**, 461 (2001).  
 [46] M. Glass-Maujean *et al.*, *Phys. Rev. A* **28**, 2868 (1983).  
 [47] D. J. Kligler and C. K. Rhodes, *Phys. Rev. Lett.* **40**, 309 (1978).  
 [48] C. W. T. Chien, F. W. Dalby, and J. van der Linde, *Can. J. Phys.* **56**, 827 (1978).  
 [49] R. L. Day, R. J. Anderson, and F. A. Sharpton, *J. Chem. Phys.* **71**, 3683 (1979).